Constitutive relations in dense granular flows

John J. Drozd and Colin Denniston
Department of Applied Mathematics, The University of Western Ontario, London, Ontario, Canada N6A 5B8
(Received 11 June 2009; revised manuscript received 23 November 2009; published 26 February 2010)

We use simulations to investigate constitutive relations in dry granular flow. Our system is comprised of polydisperse sets of spherical grains falling down a vertical chute under the influence of gravity. Three phases or states of granular matter are observed: a free-fall dilute granular gas region at the top of the chute, a granular fluid in the middle and then a glassy region at the bottom. We examine a complete closed set of constitutive relations capable of describing the local stresses, heat flow, and dissipation in the different regions. While the pressure can be reasonably described by hard sphere gas models, the transport coefficients cannot. Transport coefficients such as viscosity and heat conductivity increase with *decreasing* temperature in the fluid and glassy phases. The glass exhibits signs of a finite yield stress and we show that the static sand pile is a limit of our glassy state.

DOI: 10.1103/PhysRevE.81.021305 PACS number(s): 45.70.Mg, 83.80.Fg, 05.20.Dd

I. INTRODUCTION

The attempt to accurately describe stresses in granular matter has a long history. The problem is difficult due to the energy dissipation in the system that makes it hard for granular systems to achieve a true thermodynamic equilibrium. This makes the application of normal equilibrium statistical mechanics techniques problematic. Bagnold's early work [1] on sheared granular suspensions identified three different regimes of flow behavior, the macroviscous dominated by the interstitial fluid, the transitional, and the grain inertia regime where the effects of the interstitial fluid are negligible (similar to dry cohesionless granular materials). Savage and collaborators [2–5] worked to derive relationships based on a kinetic theory approach and describe things in terms of a dimensionless parameter R which is the ratio of mean shear characteristic velocity to the rms velocity (velocity fluctuations). Durian and Menon [6] measured a closely related quantity in a dry granular flow in a chute and found that the velocity fluctuations were proportional to the mean flow velocity to the 2/3 power (i.e. $\delta v \sim v^{2/3}$) suggesting that $R=v/\delta v$ may not be a natural parameter for granular flows [7] as it is not likely to be a constant for any particular flow. Simulations indicate that even the $\delta v \sim v^{2/3}$ is not true locally but is more a statement about global stress/energy balances (i.e., true only when suitably averaged over quite heterogeneous regions) [8]. This suggests a need to get measurements of stresses, strains, and other transport phenomena on a local level and relate them to the microscopic dynamics, something that is ideally suited to simulation studies.

The study of stresses and forces in static granular system has also been studied extensively. Force chain models [9] demonstrated the wide distribution of forces in granular packs. The consideration of the effects of directed force propagation suggests various constraints that can be placed on the stress tensor in granular packs [10–14]. Edwards and collaborators attempted to consolidate these ideas on a statistical mechanics based on an averaging over ensembles of mechanically stable packings [15,16]. This, however, is predicated on the assumption that the distribution of mechanically stable packings of spheres is relatively flat (i.e., that all mechanically stable packings are equally likely to occur). There are suggestions that this might not be the case [17]. It is therefore desirable to generate configurations in a physically meaningful way implying a coupling between the dynamics responsible for creating static states (i.e., before it became static) and the static model itself is required. Thus simulations of granular dynamics with a well defined static limit are desirable.

Phenomenological Coulomb-like friction relations, relating the shear stress to be directly proportional to the local pressure with constant of proportionality a friction coefficient χ, have been shown to be reasonably successful in describing shear flows of dense granular media in a few different geometries [18–21]. These works have attempted, with reasonable success, to parameterize the measured friction coefficients in terms of an "inertial number" R_I closely related to the number suggested by Savage, but with the velocity fluctuations replaced by $\sqrt{P/\rho_i}$, with P the pressure and ρ_i the mass density of a grain. This is essentially a recognition that the pressure in dense granular flow may be dominated by collision effects rather than velocity fluctuations. In a simple shear flow, $R_I=\dot{\gamma}a/\sqrt{P/\rho_i}$ with $\dot{\gamma}$ the shear rate, and R_I is a constant in steady-state simple shear. However, in chute flow R_I can vary by several orders of magnitude over short distances and it is not obvious that relations observed to hold in simple shear will transfer well to this geometry. Also, as yet there is not a clear relation between this phenomenological description and the microscopic dynamics.

Apart from adopting specific models, if we concentrate on the basic physics of momentum conservation, mass conservation and energy conservation, this does not provide us with enough equations to fully solve for local density, velocities, and temperature. In order to solve for these quantities, the stress tensor and heat flux need to be expressed in terms of these local variables in order to "close" the equations (i.e., have the same number of equations and unknowns). This prompts us to studying various constitutive relations to provide these necessary additional constraints. With this aim in mind, we have performed simulations of gravity driven dense granular flow in three dimensions to compare and test constitutive pressure, stress and energy relations of granular matter.

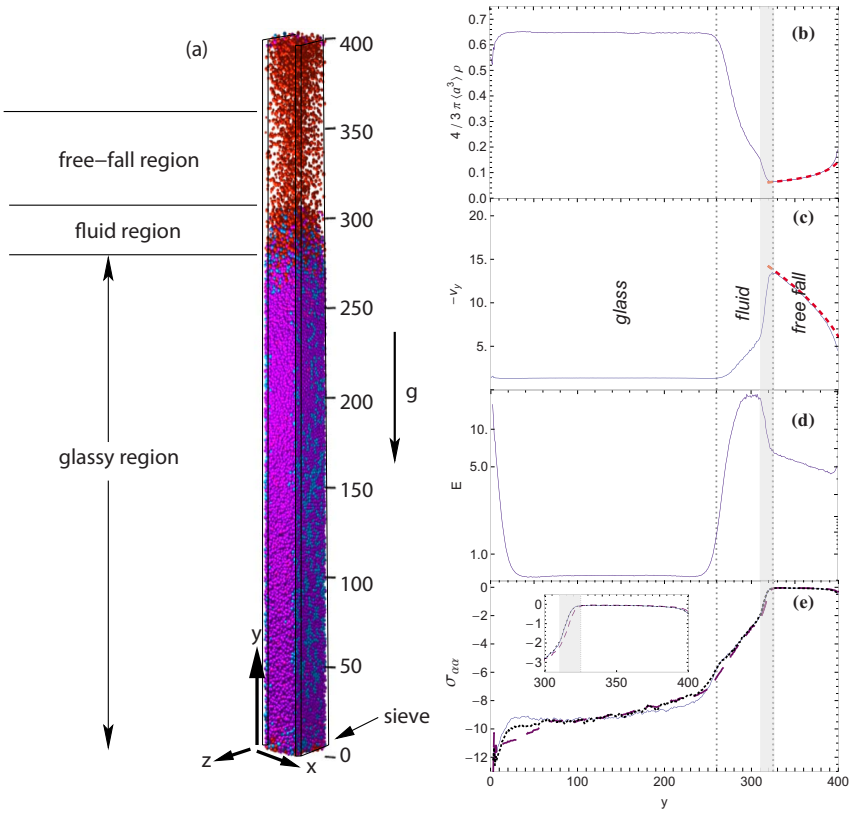

FIG. 1. (Color online) (a) Section of a simulation involving 43 200 grains with 15% polydispersity. The system size is $32a \times 32a \times 400a$. There are reflective walls at $x=0$ and $x=L_x$, periodic boundary conditions in the z direction, and a finite probability of reflection at the bottom of the chute (at $y=0$) with an asymptotic coefficient of restitution $\mu_0=0.97$. Time-averaged density (volume fraction) in (b) and $y-$ velocity in (c) down the center of a 3D chute. The short dashed lines are analytic calculations of density and v_y in the free-fall region (described in text). (d) The total kinetic energy $E=\frac{1}{2}\rho v^2+\frac{3}{2}\rho T$ and (e) stress tensor components σ_{xx} (solid line), σ_{yy} (dashed line) and σ_{zz} (dotted line). The measurements for plots (b), (c), (d), and (e) were taken down the center of the chute. Units are described in footnote [30]. For the color online version, the balls in the 3D visualization are colored according to the magnitude of vertical y velocity with the red balls being the fastest and the blue balls the slowest.

The binary, hard sphere collision model used for our simulations is similar to that used in [8,22], but for illustrative purposes a typical snapshot from one of our simulations is shown in Fig. 1(a). We will reiterate a brief description of our model in the next paragraphs but for more details one can refer to Refs. [8,22].

In our simulation, frictionless, rigid spherical grains are dropped in from the top of a rectangular chute and fall under the influence of gravity. There are flat walls at the left and right (x direction) of the chute and periodic boundary conditions at the front and back (z direction). At the bottom of the chute ($y=0$), grains are reflected with a probability p (typically $p=90\%$). Particles transmitted through the bottom are replaced at the top of the chute in order to maintain steady-state. Particles reflect off the walls of the chute with a partial loss, typically 10% in their vertical (y) velocity. This is essential as experiments show [23,24] that much of the column weight is supported by the walls.

Particles in our simulation undergo binary collisions where their momenta are transferred along the line joining their centers. Specifically, the velocities after collision $\dot{\mathbf{r}}_1'$ and $\dot{\mathbf{r}}_2'$ in terms of the velocities before collision, $\dot{\mathbf{r}}_1$ and $\dot{\mathbf{r}}_2$, are

$$\begin{pmatrix} \dot{\mathbf{r}}_1' \\ \dot{\mathbf{r}}_2' \end{pmatrix} = \begin{pmatrix} \dot{\mathbf{r}}_1 \\ \dot{\mathbf{r}}_2 \end{pmatrix} + \frac{(1+\mu)}{(m_1+m_2)} \begin{pmatrix} -m_2 & m_2 \\ m_1 & -m_1 \end{pmatrix} \begin{pmatrix} \dot{\mathbf{r}}_1 \cdot \mathbf{q} \\ \dot{\mathbf{r}}_2 \cdot \mathbf{q} \end{pmatrix} \mathbf{q}, \quad (1)$$

where $\mathbf{q}=(\mathbf{r}_2-\mathbf{r}_1)/|\mathbf{r}_2-\mathbf{r}_1|$, and μ is the coefficient of restitution. Such collision models of granular flow have a long history [5,3]. μ is a velocity-dependent restitution coefficient described by the phenomenological relation [25,26],

$$\mu(v_n) = \begin{cases} 1-(1-\mu_0)(v_n/v_0)^{0.7} & ,v_n \le v_0 \\ \mu_0 & ,v_n \ge v_0. \end{cases} \quad (2)$$

Here v_n is the component of relative velocity along the line joining the grain centers, μ_0 is the asymptotic coefficient at large velocities, and $v_0=\sqrt{2ga}$ [27]. Equation (2) effectively makes the ball collisions become more elastic as the collisions become weaker as observed experimentally [28,29]. One could adjust v_0 and the exponent in this relation to fit a specific material, but the qualitative results should be independent of v_0 as long as it is not too large. Scaled units are given in footnote [30].

In previous work [8,22] we examined both mono- and polydisperse mixtures of spheres. Here we simulate only sys-

tems with 15% polydisperse particles. In this context, a polydispersity of 15% means that the standard deviation of a particle radius is 0.15 if the mean is 1 using a Gaussian distribution of radii. Polydisperse particles achieve a truly glassy state, and here we are interested in testing and comparing constitutive relations in the glassy state, in addition to the free-fall and fluid states. Monodisperse or nearly monodisperse particles experiencing shear often increase in order and crystallize [8,22,31], and it is beyond the scope of this paper to examine the approach to the crystallized state in detail, although we did touch upon such details in previous work [8,22].

A typical steady-state configuration of our simulation is shown in Fig. 1(a). The steady-state density (plotted as a volume fraction), velocity, energy, and diagonal stresses from our simulation for this typical configuration were measured all down the center of the channel and are plotted in Figs. 1(b)–1(e), respectively. The orientation of the x, y, and z axes is shown at the bottom of the visualization in Fig. 1(a).

As indicated by the labels and vertical dashed lines in Figs. 1(b)–1(e), there are three regions, which we label as a glassy region, a fluid region and a free-fall region. These labels were justified in our previous work [8,22]. In the free-fall region the grains accelerate at $1g$ and collisions do not have a significant impact on their kinetics [8,22]. In the liquid region the density is sufficiently high that collisions mix the grains, but the distribution of collision times are exponential, meaning that collisions are largely independent. In the glass region, the collision time distribution is a power-law and thus collisions are not independent and as a result there are collisions at a wide range of time scales [22].

It is important to note that the relative sizes of the glassy, fluid and free-fall regions vary depending on the coefficient of restitution used. As expected, the lowest asymptotic coefficient of restitution of 0.9 resulted in the smallest fluid region, an intermediate asymptotic coefficient of restitution of 0.95 resulted in a larger fluid region, and the largest asymptotic coefficient of restitution of 0.99 resulted in the largest fluid region for the same sized column. The existence of transition regions between the free-fall, fluid, and glassy states was demonstrated in previous work [8]. The transition region between the free-fall region and the fluid region is indicated by the vertical gray shaded stripe in Figs. 1(b)–1(e). Unless noted, the results shown in this paper use an asymptotic coefficient of restitution of 0.97 so we can study one of the wider transition regions. A wider fluid region clearly shows a kink in the free-fall to fluid transition region in the data profiles as shown in Figs. 1(b)–1(e). It is interesting to note that the kink at this transition in the density and velocity profiles lines up with the peak in the kinetic energy and inflection point in the stress profiles as shown in Figs. 1(d) and 1(e). This peak marks the boundary between the fluid region and the free-fall to fluid transition region.

II. CONTINUUM EQUATIONS

Our simulation evolves over discrete binary collisions. In our simulation, we average various physical properties based on these discrete events over time and space. We resolve our $32a \times 32a \times 400a$ chute over a fine volume grid composed of $1a \times 1a \times 1a$ cubes. This resolution was chosen to scale with the size of the particles of mean radii $a=1$. This allows us to map our discrete system onto a time-averaged continuum set of fields. We will now begin by describing the continuum equations describing the average density, $\langle \rho \rangle$, velocity $\langle \vec{v} \rangle$, and energy $\langle E \rangle$ that we would expect our system to map onto. To simplify the notation, even though the measured properties in our simulation are quantities averaged in time and over the translational invariant z direction, we omit the angled brackets $\langle \cdot \rangle$ in the conservation equations that follow. Typical averaging times are 600 to 1000 time units after 200 time units of equilibration. The equilibration time of 200 time units is equivalent to the typical lifetime of a particle in the chute for the slower moving systems (i.e., the time from when it enters at the top to falls out the bottom).

A. Conservation equations

In this section, we will describe the continuum equations of conservation of mass, momentum, and energy that we will attempt to map our simulation results onto. We will describe how the physical terms in these equations can be measured directly from our simulation.

The continuity equation for mass gives us one equation

$$\frac{\partial \rho}{\partial t} + \nabla \cdot (\rho \mathbf{v}) = 0. \tag{3}$$

Momentum conservation requires that

$$\partial_t(\rho v_\alpha) + \partial_\beta(\rho v_\alpha v_\beta) = \partial_\beta \sigma_{\alpha\beta} + \rho g_\alpha, \tag{4}$$

where $\sigma_{\alpha\beta}$ is the stress tensor, and all v_α and v_β refer to first moments of the velocity distribution. This gives us three Navier-Stokes equations.

The time-averaged stress tensor can be directly measured in our simulation using the microscopic form of the three-dimensional (3D) stress tensor [32],

$$\sigma_{\alpha\beta} = \sigma_{\alpha\beta}^{\text{kinetic}} + \sigma_{\alpha\beta}^{\text{collision}}, \tag{5a}$$

$$= -\langle \rho (v_\alpha - \langle v_\alpha \rangle)(v_\beta - \langle v_\beta \rangle) \rangle + \frac{1}{t} \sum_{collisions} - \frac{1}{2}(1+\mu)(\dot{\mathbf{r}}_1 - \dot{\mathbf{r}}_2) \cdot \hat{\mathbf{q}}(\hat{\mathbf{q}} \cdot \hat{\mathbf{e}}_\alpha)(\hat{\mathbf{q}} \cdot \hat{\mathbf{e}}_\beta). \tag{5b}$$

The $\frac{1}{2}$ accounts for the double counting of collisions in the sum (we count the transfer from particle 1 to 2 and the transfer from 2 to 1).

Our fifth equation is an equation describing the energy conservation in our system

$$\partial_t(E) + \partial_\alpha(v_\alpha E + F_\alpha) = I + \rho g \cdot \mathbf{v} \tag{6}$$

The (kinetic) energy is

$$E = \frac{1}{2}\rho v^2 + \frac{3}{2}\rho T. \tag{7}$$

Note that $v^2 = \langle v \rangle^2$ in the first term and

$$T = \frac{1}{3}\delta v^2 = (\langle v_x^2\rangle + \langle (v_y - \langle v_y\rangle)^2\rangle + \langle v_z^2\rangle)/3 \tag{8}$$

is the granular temperature. The energy, E, from our simulation is plotted in Fig. 1(d). $\mathbf{F}$ is the nonconvective energy flux and α refers to the x, y, or z component.

An important component of the nonconvective energy flux $\mathbf{F}$, is the collision energy flux, $\mathbf{F_c}$. Part of the energy flux is related to the coherent transfer of momentum, that is, the work done by the stress tensor and the other part is the heat flux. We can measure the energy transferred between grains in a collision using Eq. (1) [32] to get

$$\boldsymbol{\delta}\mathbf{F_c} = \frac{1+\mu}{m_1+m_2}[m_1(\dot{\mathbf{r}}_1\cdot\mathbf{q})^2 - m_2(\dot{\mathbf{r}}_2\cdot\mathbf{q})^2]\mathbf{q}. \tag{9}$$

Averaging over time gives the collision energy flux as

$$\mathbf{F_c} = \frac{1}{t}\sum_{collisions}\boldsymbol{\delta}\mathbf{F_c}. \tag{10}$$

Similarly, we can easily use Eq. (1) to calculate the dissipation, I from the kinetic energy lost in each collision,

$$\delta I = -\frac{1-\mu^2}{2(m_1+m_2)}(m_1\dot{\mathbf{r}}_1\cdot\mathbf{q} - m_2\dot{\mathbf{r}}_2\cdot\mathbf{q})^2. \tag{11}$$

If we average δI over the collisions that occur in a small cell $(1\times 1\times L_z)$ of our simulation, and if we also average δI per unit time (effectively multiplying by the collision frequency f_c), we arrive at the average dissipation rate I which is the remaining term in Eq. (6).

Equations (3), (4), and (6) give us five equations (in the static limit), but there are six unknown stress values, namely, the diagonal stresses σ_{xx}, σ_{yy}, σ_{zz}, and using the fact that the stress tensor is symmetric, we have the shear stresses $\sigma_{xy}=\sigma_{yx}$, $\sigma_{xz}=\sigma_{zx}$ and $\sigma_{yz}=\sigma_{zy}$. We need six constitutive equations to solve for these six unknown stress values. Similarly, all the terms in Eq. (6) can be measured directly from a simulation, however they cannot be predicted ahead of time without relating the $\mathbf{F}$ and I to the density, velocities, or energy by means of two additional constitutive relations. The dissipation and heat flux will be examined in more detail in Sec. II G.

B. Stress and energy balance

In the previous section we described the conservation equations that are applicable to our system. In the upcoming sections we will examine these conservation equations in detail applying them to the different regions of our simulation. In this section we will examine the balance of stress and energy in the fluid, glass and free-fall regions.

First examine Eq. (4) in the liquid and glassy regions. The stress tensor cannot be ignored in these regions, even as a first approximation. If we assume in Eq. (4), that the time derivative is zero as we are in steady state, and if we assume that the kinetic terms, $\partial_\beta(\rho v_\alpha v_\beta)$ are negligible (as is observed by the low acceleration values in the glassy and in part of the fluid region in Fig. 2(c) in Ref. [8] and in Fig. 1(d) in Ref. [22]), we arrive at

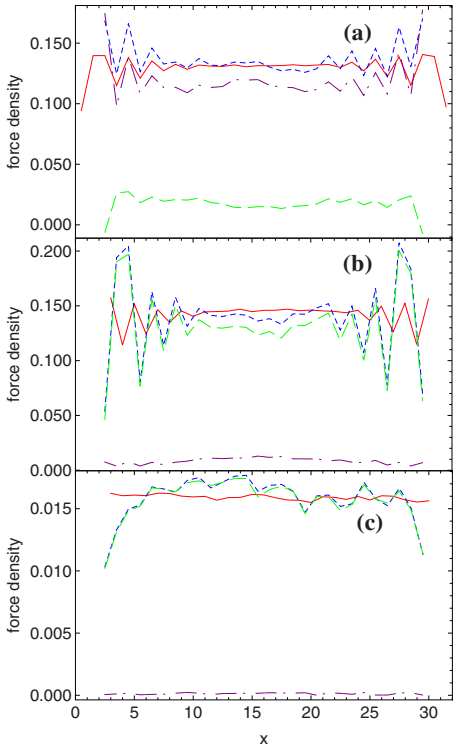

FIG. 2. (Color online) Plot of force densities $\partial_y\sigma_{yy}$ (dot-dashed line), $\partial_x\sigma_{yx}$ (long dashed line), $\partial_x\sigma_{yx}+\partial_y\sigma_{yy}$ (short dashed line) and the weight $-\rho g_y$ (solid line) in (a) the fluid region and (b) the glassy region versus the width x for a 400-height column using an asymptotic coefficient of restitution μ_0 of 0.97 and probability of reflection $p=90\%$. (c) Plot of force densities $\partial_y\sigma_{yy}$ (dot-dashed line), $-\partial_y\rho v_y^2$ (long dashed line), $(\partial_x\sigma_{yy}-\partial_y\rho v_y^2$ (short dashed line) and the weight $-\rho g_y$ (solid line) in the free-fall region. Units are described in footnote [30].

$$\partial_x\sigma_{yx} + \partial_y\sigma_{yy} = -\rho g_y, \tag{12}$$

where $g_y=-g<0$ in this orientation.

Figures 2(a) and 2(b) show the balance of the weight, $-\rho g$ and stress gradients $\partial_x\sigma_{yx}+\partial_y\sigma_{yy}$ in the fluid and glassy regions, respectively. There are *very* significant differences between how these terms are balanced in the liquid and glassy regions. We find that the pressure gradient $\partial_y\sigma_{yy}$ is the dominant term supporting the weight in the fluid region. This is consistent with what one would expect in a simple fluid where the pressure would be a function of depth, $P=\rho g y+$constant. In contrast, in the glassy region we find that the gradient in the shear stress, $\partial_x\sigma_{yx}$ is the dominant term supporting the weight. Here, as in [22], we can conclude that in the glassy region the system supports a finite shear stress and this region behaves like a solid in this sense.

Now that we have looked at the stress balance in the fluid and glassy regions, we examine the balance in the free-fall region. Taking the y component of the Navier-Stokes equation (4), we have

$$\partial_y(\rho v_y^2) = \partial_y\sigma_{yy} + \rho g_y, \tag{13}$$

where $g_y=-g<0$ in this orientation. Figure 2(c) shows the balance of the weight, ρg and stress gradients

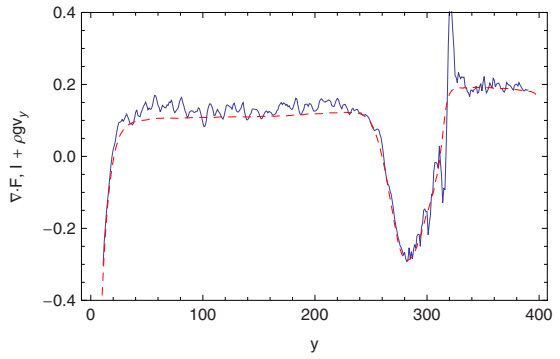

FIG. 3. (Color online) (a) The components of the energy equation from Eq. (14) in the free-fall region. The solid line is the left side of the equation, $\nabla \cdot \mathbf{F}$, and the dashed line is the right side of the equation, $I+\rho g v_y$. Units are described in footnote [30].

$\partial_y \sigma_{yy} - \partial_y(\rho v_y^2)$. In the free-fall region the pressure gradient, $\partial_y \sigma_{yy} \approx 0$, and the kinetic term, $-\partial_y(\rho v_y^2)$, contributes solely to balance the weight, ρg.

Finally, we explore the energy balance Eq. (6) in all three regions. We can assume that the time partial derivatives are negligible since we are in steady state and that the derivatives in the periodic z direction are also negligible. Note that the only significant energy fluxes are in the x and y directions and $\delta v_x^2 \approx \delta v_y^2 \approx \delta v_z^2$ and thus we can say that $T \approx \delta v_y^2$ (the isotropic assumption is not strictly correct but is a reasonable first approximation in the bulk regions [8]). Using these assumptions together with Eq. (6), we finally arrive at the energy equation

$$\nabla \cdot \mathbf{F} = I + \rho g v_y, \tag{14}$$

where we have used the following relation to separate the kinetic and collision energy flux [4]:

$$\mathbf{F} = \mathbf{F_c} - \frac{1}{2}\langle \rho (v_\alpha - \langle v_\alpha \rangle)(v_\beta - \langle v_\beta \rangle)\rangle v_\beta. \tag{15}$$

The left and right sides of Eq. (14), as directly measured from our simulation, are plotted in Fig. 3. The clear agreement in the free-fall, fluid, and glass regions shows that all the assumptions made to this point are reasonable.

Thus we see that particularly the stress balance distinguishes the different states of the system but in order to actually solve the conservation equations we need to relate the measured stress, dissipation, and energy flux to the density, velocities, and granular temperature. This is the focus of the rest of the paper.

C. Pressure

In our discussion of stress balance in the previous section, we demonstrated the role of the pressure gradient in balancing the weight, particularly in the fluid and somewhat less importantly in the glass. In this section, we will examine several equations of state for pressure for the glassy and fluid regions of our system. In a simple fluid the pressure is normally defined as

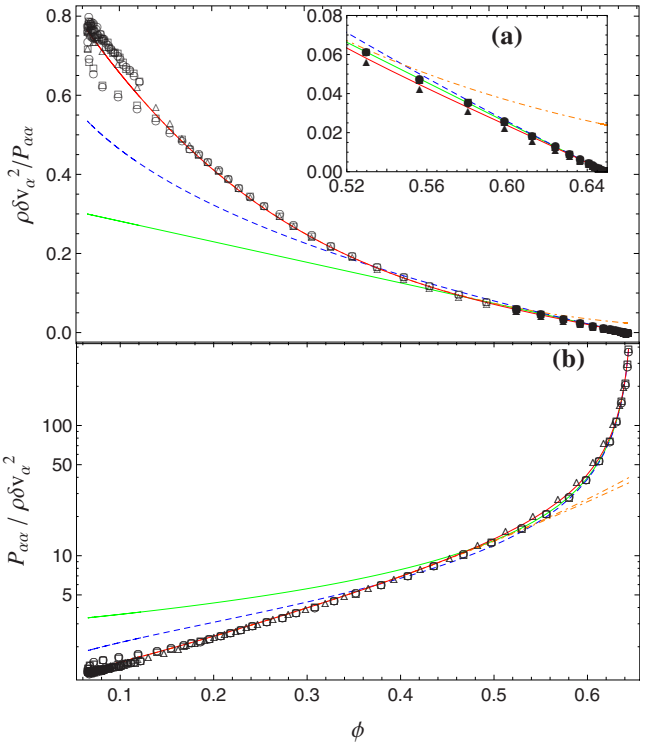

FIG. 4. (Color online) (a) Plot of $\rho \delta v_x^2 / P_{xx}$ (squares), $\rho \delta v_y^2 / P_{yy}$ (triangles), and $\rho \delta v_z^2 / P_{zz}$ (circles) versus ϕ. Also plotted are the result from Eq. (19) [solid green (bottom) line], Eq. (18) [blue dotted (middle) line], and Eq. (23) [orange dot-dashed (top) curve]. ϕ_c is the observed close-packed density in the glassy region and $\delta v_\alpha^2 = \langle (v_\alpha - \langle v_\alpha \rangle)^2 \rangle$. (b) Inverse of data in (a). In both plots closed symbols indicate the glassy region and open symbols the fluid regions. The data are for a $32 \times 32 \times 400$ simulation with an asymptotic coefficient of restitution $\mu_0 = 0.97$ and a probability of reflection at the bottom of the chute $p = 0.9$. The red curve through the data are described in the text.

$$P = -\frac{1}{3} Tr(\boldsymbol{\sigma}), \tag{16}$$

and the diagonal stresses $\sigma_{\alpha\alpha} = -P$. However, as is already clear from Fig. 1(e) the diagonal stresses are not equal everywhere, so we will examine the pressure tensor diagonal components as

$$P_{\alpha\alpha} = -\sigma_{\alpha\alpha}. \tag{17}$$

As jamming is approached, Salsburg and Wood [33] used a free volume approximation to suggest that the pressure in a classical (conservative) hard sphere system approaches

$$P = (\rho T)(1 - (\phi/\phi_c)^{1/D})^{-1}, \tag{18}$$

They also gave an asymptotic approximation (as $\phi \to \phi_c$) of Eq. (18) as

$$P = D(\rho T)(1 - \phi/\phi_c)^{-1}. \tag{19}$$

In Eqs. (18) and (19) D is the dimension and ϕ is a volume packing fraction

$$\phi = \frac{4}{3}\pi\langle a^3\rangle\frac{\rho}{m}, \tag{20}$$

where m is a mean grain mass, and ϕ_c is a random close-packed density (the mean of the cube of the radius is used here rather than the mean radius cubed). For monodisperse spheres, ϕ_c is known to be ~ 0.64. As our spheres are polydisperse ϕ_c is unknown and must be fit. Typically it is slightly higher than the monodisperse case at 0.65. Normally these expressions involve Boltzmann's constant and the absolute temperature, which is not relevant for dissipative granular materials so we follow standard convention and replace k_BT with the granular temperature in Eq. (8), something that would be entirely equivalent in a conservative hard sphere system. Also, the true form of Eq. (19) has an additional constant of order 1, but literature usually quotes this equation suppressing the constant.

As can be seen in Fig. 4 both Eqs. (18) and (19) do well as the close-packed density is approached in the glassy region, but they give higher pressures than what we observed in our simulation at lower densities in the fluid regions. As expected, the asymptotic approximation Eq. (19) is worse in the fluid region than the true free-volume expression Equation (18), although both disagree with our simulation data in the fluid region. Similar effects are found in simulations of elastic hard sphere packings [34].

At low densities, a more appropriate approach to studying the equation of state of a hard sphere fluid is to use a virial expansion,

$$\frac{P}{\rho T} = 1 + B_2\phi + B_3\phi^2 + \ldots, \tag{21}$$

where again ϕ is the volume packing fraction proportional to density and B_i are the virial coefficients. For hard spheres, the Carnahan-Starling [35] equation of state for a hard sphere fluid uses a rescaled virial series solution of the Percus-Yevick equation [36] for hard spheres which is an approximate integral equation for determining the radial distribution function of a fluid. It uses the rescaled virial series

$$\frac{P}{\rho T} = \frac{1 + c_2\phi + c_3\phi^2 + \ldots}{(1-\phi)^3}, \tag{22}$$

where c_i are related to the virial coefficients B_i. The Carnahan-Starling [35] equation of state is written as

$$\frac{P}{\rho T} = \frac{(1 + \phi + \phi^2 - \phi^3)}{(1-\phi)^3}. \tag{23}$$

Both the Carnahan-Starling equation, Eq. (23), as well as the virial expansion to 12 coefficients, as derived in [37,38], are shown in Figure 4 [dash-dotted lines, indistinguishable from each other except at high densities in Fig. 4(b)] and agree well with our data in the lower density fluid region. In the literature, there are several other equations of state that are proposed as solutions to the Percus-Yevick equation which are slightly more accurate than the Carnahan-Starling equation. Examples of these include the Kolafa equation [39] and the Malijevsky and Veverka equation of state [40]. The Malijevsky and Veverka equation, for instance, uses a combination of the analytical solution of the Percus-Yevick equation and a Pade approximation of the rescaled virial series using the first seven virial coefficients to improve the convergence of the virial expansion. When we plotted the Kolafa and Malijevsky and Veverka equations of state we found that these solutions were very close to the Carnahan-Starling equation of state and gave no significant improvement in agreement with our data.

The close agreement between the virial/Carnahan-Starling result and our data is surprising. These theoretical results are based on the assumption that the grains are in a thermal equilibrium which would be characterized by a Gaussian distribution of velocities. In contrast to a conservative hard sphere fluid, a dissipative granular fluid does not form a Gaussian velocity distribution. Experiments [41,42], theory [43–45], and simulations [8] have shown that in a granular fluid, the distribution of velocity fluctuations is not Gaussian. At low v_x, the v_x distribution fits a Gaussian but has stretched exponential tails. These tails gradually fill the whole distribution such that the entire distribution can be well fit with a 1.5 power law instead of the power-law exponent of 2 that would be expected for a Gaussian velocity distribution [8]. The lack of normal thermal equilibration is also particularly evident in the free-fall to fluid transition area [the low density region in Fig. 4(b)]. Here the P_{yy} data match the Carnahan-Starling equation and the virial expansion, but P_{xx} and P_{zz} do not. This indicates that in this transition region, the fluid is not fully equilibrated in the x-x and z-z directions. Thus we should not expect that Eq. (23) and the coincident virial expansion can be directly applied to a granular fluid. However, surprisingly the Carnahan-Starling and the virial expansion work extremely well in the fluid region, matching our simulation data. A reason may be that even though in the velocity distribution the 1.5 power law exists in the tails, the distribution still remains Gaussian in the center. This implies that the pressure in the fluid and free-fall region is not too sensitive to the tail distribution.

It is also remarkable that there is no real signature of the different phases in the pressure. The ratio of $P/(\rho T)$ diverges as close packing is approached but is still finite throughout the glassy region. As we shall see below, these phases are only distinct when we consider dynamic properties such as transport coefficients. This fits with the usual description of the glass transition being a dynamical transition. What is perhaps more interesting is that the free-fall to fluid transition must also be a dynamic transition if these phases are truly distinct. We will examine this in more detail in later sections.

An asymptotically matched expression that interpolates between the virial and the free-volume expression for the pressure can be found by taking the virial expansion up to and including $B_5\phi^4$ and adding to it Eq. (18) and subtracting the Taylor series expansion of Eq. (18) taken about $\phi=0$ up to and including the ϕ^4 term:

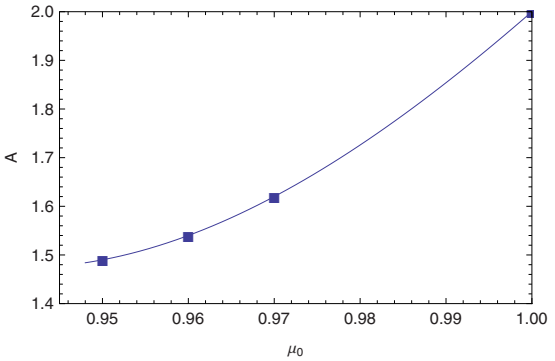

FIG. 5. (Color online) Plot of the empirically determined parameter A in Eq. (30) for the glassy region of the chute from simulations with different asymptotic coefficients of restitution μ_0. The line is just a guide for the eyes.

$$\frac{P}{\rho T} = (1 + B_2\phi + B_3\phi^2 + B_4\phi^3 + B_5\phi^4) + \left[1 - \left(\frac{\phi}{\phi_c}\right)^{1/3}\right]^{-1} - \sum_{n=0}^{n=12}\left(\frac{\phi}{\phi_c}\right)^{n/3}. \quad (24)$$

This is shown in Fig. 4 as the solid red line that goes through the simulation data.

D. Collision frequency

Many of the constitutive relations derived in following sections, such as for the dissipation and energy flux, will involve a collision frequency (per unit volume). Thus, it seems appropriate to first establish closed relations for the collision frequency, f_c that are valid in the different regions. As we will show below, a closed relation for the collision frequency can be found from the expression (5) for the stress measured in the simulation and the fact that Eq. (24) expresses the pressure in the different regions in terms of the density and temperature.

We use the sign convention for the pressure tensor $P_{\alpha\beta}=-\sigma_{\alpha\beta}$. The virial can be defined from the stress as

$$V = -\frac{1}{3}Tr(\sigma_{\alpha\beta} - \langle\rho(v_\alpha - \langle v_\alpha\rangle)(v_\beta - \langle v_\beta\rangle)\rangle), \quad (25a)$$

$$\approx P - \rho T, \quad (25b)$$

where the pressure P is a function of the density ρ and granular temperature T as detailed in the previous section. The kinetic term in Eq. (25a), $\langle\rho(v_\alpha-\langle v_\alpha\rangle)(v_\beta-\langle v_\beta\rangle)\rangle$, is negligible in the glass but is significant in the fluid and free-fall regions.

Using Eq. (4) we also have the relation

$$V = \frac{1}{2}f_c\langle(1+\mu)(\dot{\mathbf{r}}_1 - \dot{\mathbf{r}}_2)\cdot\mathbf{q}\rangle,$$

$$= f_c\langle 1+\mu\rangle\langle v_n\rangle, \quad (26)$$

where

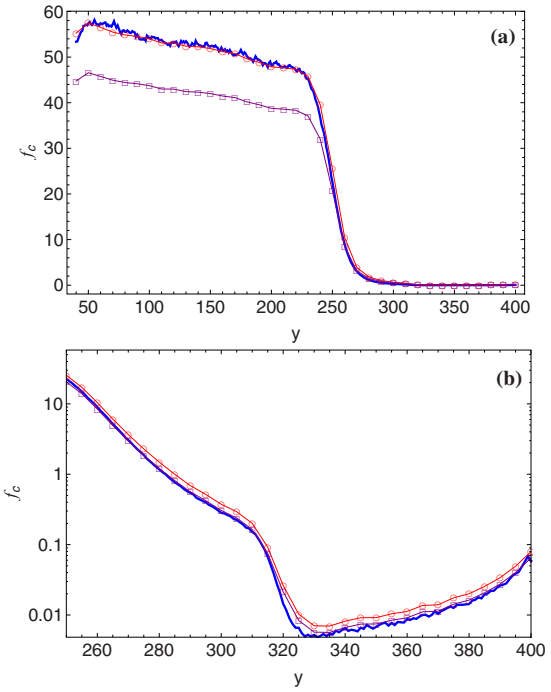

FIG. 6. (Color online) Plot of the collision frequency per unit volume as calculated using Eq. (31) using $A=1.62$ (red line with ○'s), as calculated using Eq. (31) using $A=2$ (purple line with □'s), and the simulation values for the collision frequency (blue solid line) versus the height y of the chute in (a) the entire chute and (b) in the fluid region (semilogarithmic). Measurements are taken in the center of the chute using a simulation with an asymptotic coefficient of restitution $\mu_0=0.97$. Data are averaged over depth ($32a$) in z and over 800 time units. Units are described in footnote [30].

$$(\dot{\mathbf{r}}_1 - \dot{\mathbf{r}}_2)\cdot\mathbf{q} = \mathbf{v_n} \quad (27)$$

is simply the normal impact velocity between the colliding particles and the factor of 1/2 disappeared because it was due to the double counting in the average over collisions (which counts the momentum transferred from particle 1 to 2 and from particle 2 to 1 in) and this is not present in the second line.

By combining Eqs. (25a) and (26) we have

$$f_c = \frac{3V}{\langle 1+\mu(v_n)\rangle\langle v_n\rangle}, \quad (28)$$

$\mu(v_n)$ is the velocity-dependent coefficient of restitution given by Eq. (2).

During a collision the sign of v_n is fixed and v_n is always positive, as can be readily seen from Eq. (27). In Ref. [8], we showed that v_n^2 traces the velocity fluctuations δv_α^2. Thus we expect $\langle v_n\rangle$ to be related to $\langle|\delta v_\alpha|\rangle$,

$$\langle|\delta v_\alpha|\rangle = \sqrt{\frac{2}{\pi}}\langle\delta v_\alpha^2\rangle^{1/2}, \quad (29)$$

if δv_α is distributed in a Gaussian. This is nearly true in the liquid and free-fall regions. However, δv_α is not strictly distributed in a Gaussian distribution in the glassy region. If the particles are moving statistically independently

$$\langle v_n \rangle = \sqrt{\frac{2}{\pi}} A T^{1/2}, \tag{30}$$

where $A=2$ in the liquid and free-fall regions. In the glassy region $P(\delta v)$ is *not* Gaussian [8] and the particles are not moving or colliding independently [8,22]. So $\langle v_n \rangle_{\text{collisions}} \neq \langle \delta v \rangle_{\text{particles}}$. Thus in the glass, $A<2$ and a value for A has to be determined empirically. For an asymptotic coefficient of restitution of $\mu_0=0.97$, we found $A=1.62$ in the glass. Figure 5 shows a plot of A in the glassy region for three different coefficients of restitution. As the simulation becomes more elastic, that is as $\mu_0 \to 1$, $A \to 2$.

We also calculated A in the glassy region for simulations with different sieve probabilities, hence for different flow rates with the same asymptotic coefficient of restitution, and found that A did not vary with the flow rate in the glassy region.

Upon combining, Eqs. (2), (28), and (29), we finally arrive at closed expression for the collision frequency f_c,

$$f_c = \frac{3V}{\left[2-(1-\mu_0)\left(\frac{\sqrt{\frac{2}{\pi}}AT^{1/2}}{v_0}\right)^{0.7}\right]\sqrt{\frac{2}{\pi}}AT^{1/2}}, \tag{31}$$

with A as defined for the different regions in the paragraph above. We have used the fact that in the glass the normal velocity, v_n, is less than the cutoff velocity $v_0=\sqrt{2ga}$ [27]. Figure 6 shows that the collision frequency as calculated using Eq. (31), and the collision frequencies obtained from the simulation agree nicely. To use this expression in one of the continuum relations, the virial V would need to be calculated using Eqs. (24) and (25b) which give V in terms of density and temperature.

E. Conservation equations in free-fall region

In this section, we will examine properties in the free-fall region which we can solve for analytically. In the free-fall region, the stresses are very small, and their gradients even smaller. As can be seen in the flat pressure profile in the free-fall region in the inset in Fig. 1(e), there is a small (mostly kinetic) stress contribution. This allows us to greatly simplify the above equations and solve for the density, velocity and energy in the free-fall region. As described in Ref. [8], the fluid region starts as a boundary layer in the free-fall region which gradually grows to dominate the flow. As such, what we describe in this section just applies to the pluglike flow in the central (away from the walls) portion of the channel. In this pluglike flow region, velocity gradients in the x-direction are negligible {e.g., see Fig. 3(b) in Ref. [8]}, as are shear stresses σ_{xy}. Due to the periodic boundary conditions in the z-direction physical properties are translational invariant, on average, along z. Our system is in a steady state so we can also assume that the partial derivative with respect to time in Eqs. (3), (4), and (6) are negligible.

With these assumptions in the free-fall region, the Continuity Eq. (3) translates to:

$$\partial_y(\rho v_y) = 0. \tag{32}$$

and the y component of the Navier-Stokes Eq. (4) translates to

$$\partial_y(\rho v_y^2) = \partial_y \sigma_{yy} + \rho g. \tag{33}$$

There is a very small kinetic contribution to the stress as can be seen in the inset in Fig. 1(e),

$$\sigma_{yy} = -\rho \delta v_y^2. \tag{34}$$

However this kinetic stress contribution in the free-fall region is nearly constant (except close to the inlet) as can be seen by the horizontal profile in the inset in Fig. 1(e), and thus

$$\partial_y \sigma_{yy} = -\partial_y \rho \delta v_y^2 \approx 0. \tag{35}$$

We can then solve for the density and velocity in the free-fall region using Eqs. (32) and (33) and one data point in the bulk interior of the free-fall region at a height y_0, at mid-width (mid x direction) and mid-depth (mid z direction) in the chute. The reason we use an interior point as opposed to a boundary value, say at the top of the chute is because the assumption of σ_{yy} being constant is most true once the grains have moved a finite distance into the chute. This is not strictly a required assumption to solve the equations, but it is required if we wish to solve without consideration of the energy equation.

Thus solving Eqs. (32) and (33), gives us the solution

$$\rho = c/v_y, \tag{36}$$

$$v_y \approx -\sqrt{2gy + k_1}, \tag{37}$$

where the constants are

$$k_1 = v_{y_0}^2 - 2gy_0, \tag{38}$$

$$c = \rho_{y_0} v_{y_0}, \tag{39}$$

where ρ_{y_0} and v_{y_0} are from any single point in the interior of the free-fall region as described in the previous paragraph. Equations (36) and (37) are plotted as dashed lines in the free-fall region in Figs. 1(b) and 1(c). The agreement between the analytical results and the simulation in the free-fall region is remarkably good. Not surprisingly, there is some deviation at the very top of the chute where the approximation that $\sigma_{yy} \approx$ constant breaks down. As we noted above, in the free-fall region the stress is almost entirely from the kinetic terms so that $\sigma_{yy}=-\rho\delta v_y^2$ so to improve our analytic solution we must examine the energy equation (to obtain a better solution for δv_y^2).

It is clear however, that to solve these equations analytically (or numerically without input from the simulation) that constitutive relations giving I and F_c are needed. These will be presented in Sec. II G.

F. Shear-stress constitutive relations: Models of viscosity

In Refs. [8,22], it was demonstrated that the velocity profile of particles in the fluid region was parabolic (Poiseuille

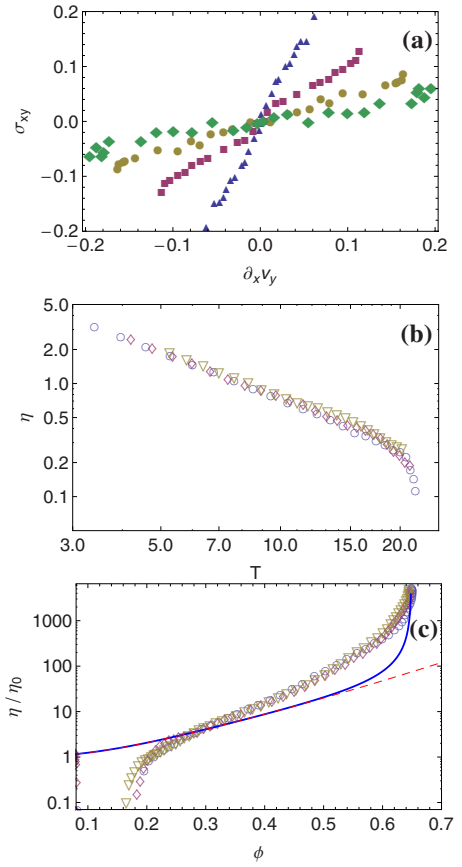

FIG. 7. (Color online) (a) Shear stress σ_{xy} versus shear rate $\partial_x v_y$ in the fluid region for a slow flow. Lines connect data at fixed heights in the fluid region (▲'s at $y=277$, ■'s at $y=283$, ●'s at $y=289$ and ◆'s at 295) and each symbol is from a local measurement at a different x (probability of reflection at the bottom sieve of p=90%, $\mu_0=0.95$ in all cases). (b) Log-log plot of viscosity in the fluid region [slope of each line in (a)]. Symbols indicate different asymptotic coefficients of restitution, μ_0 (with ○'s using $\mu_0=0.95$ and $p=90\%$, ◇'s using $\mu_0=0.96$ and $p=90\%$, and ▽'s using $\mu_0=0.97$ and $p=90\%$). Systems with the higher asymptotic coefficients of restitution of $\mu_0=0.95$, 0.96 and 0.97 achieve a true fluid region and have a consistent power-law of $-\frac{4}{3}$.) (c) Same data as (b) but scaled by η_0 from Eq. (42) and ploted versus volume fraction ϕ. The lines in (c) are from the Enskog prediction, Eq. (43) as explained in the text. Units are described in footnote [30].

flow), but as one approached the glassy region a plug type profile emerged. The development of this plug profile in the y velocity was clearly correlated with the center region solidifying into a glass. As the particles travel down the chute, they are slowed by the drag force at the walls supporting the weight of this glassy region via a shear stress. This gives a pluglike profile. We cannot overemphasize the important role that the shear stress has on the y-velocity profiles for particles traveling from the fluid to a glassy region. The stresses were shown to be crucial in providing the weight balance that we discussed in Sec. II B. In this section, we will discuss constitutive relations for the shear stress in the fluid and glassy regions of our granular system.

Most works based on kinetic theory assume a fluidlike constitutive relation for the shear stress in the system

$$\sigma_{xy} = \eta \partial_x v_y, \tag{40}$$

where σ_{xy} is the shear stress, η is the effective viscosity and $\partial_x v_y$ is the shear rate. The difficulty with such descriptions is that the viscosity η is strongly dependent on things like the granular temperature which varies considerably in space in many granular systems.

This complexity can be seen in Fig. 7(a) which plots the shear stress σ_{xy} versus the shear rate $\partial_x v_y$ in the granular fluid region along x and at different heights (i.e. each line is at a fixed height and each symbol on the line is from a different value of x at that height where the shear stress and strain rate are locally measured). Here, it was important to use a slow ($p=90\%$) system with a high enough asymptotic coefficient of restitution $\mu_0=0.95$ in order to achieve a true fluid region of study. The temperature in this region is fairly uniform in width x but changes dramatically in height y (see Figs. 5 and 6 in Ref. [8]). We plotted the shear stress σ_{xy} versus the shear rate $\partial_x v_y$ for different heights, hence at different temperatures, as shown in Fig. 7(a). Fig. 7(a) does display the linear relation of Eq. (40). To calculate the viscosity η, we then measured the slopes of σ_{xy} versus $\partial_x v_y$ at these different heights, and plotted these viscosity values versus the granular temperature T at these heights. We obtained a power-law relationship between the viscosity and the granular temperature along heights in the fluid region as shown in Fig. 7(b).

$$\eta \sim T^{-4/3}. \tag{41}$$

Equation (41) for the fluid region at first seems surprising. If you recall, in Sec. II C, particularly by looking at Fig. 4, we were able to successfully match the pressure in the fluid region from our simulation to the pressure equation of state obtained from a virial expansion. Thus it would be logical that one should expect our fluid, at least at the lower densities, to behave as a hard sphere gas whose viscosity as given from any standard textbook [46] would be

$$\eta_0 = \frac{5}{64}\frac{1}{a^2}\sqrt{\frac{mT}{\pi}}. \tag{42}$$

One can see from Eq. (42), for a hard sphere gas, the viscosity $\eta \sim T^{1/2}$. Thus one would expect the viscosity to increase with temperature, but from Eq. (41) and the corresponding Fig. 7(b), the viscosity actually decreases with increasing temperature. This is not how a typical gas behaves. This behavior is often associated with a liquid whose viscosity grows larger as the temperature goes down as you approach the solid state. The density also increases as we go from a gas to liquid to solid state and the Enskog expansion for higher density for elastic hard spheres that gives the viscosity as a function of density is [47],

$$\frac{\eta}{\eta_0} = 4\phi\left(\frac{1}{Z} + 0.8 + 0.761Z\right), \tag{43}$$

where $Z=P/(\rho T)-1$. This is shown in Fig. 7(c) with the dashed line being the expectation from using the virial expansion for P while the solid line is from using Eq. (24) for P. Except at a single density (in the liquid, around $\phi=0.27$), the Enskog expansion does not agree with the measured vis-

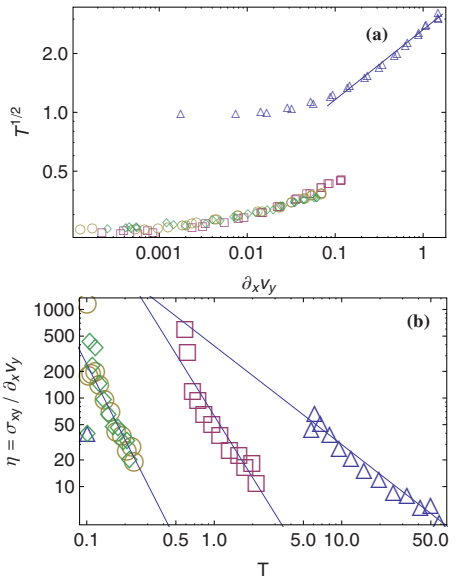

FIG. 8. (Color online) (a) Log-Log plot of square root of temperature versus shear rate in the shear zones along the walls of the glassy region. A system with a fast flow (probability of reflection at the bottom sieve of $p=1\%$, △ and $\mu_0=0.9$) yields a region with the experimental power-law exponent of 0.4 (line), while slow systems (probability of reflection at the bottom sieve of $p=90\%$ with $\mu_0=0.9$ □, $\mu_0=0.95$ ○, $\mu_0=0.96$ ◇, and $\mu_0=0.97$ ▽) have a pseudo-power-law with exponent 0.2. (b) Log-log plot of effective shear viscosity $\eta=\sigma_{xy}/\partial_x v_y$ versus temperature T in the glassy region for a fast flow (△) and slower flows [symbols same as in (a)]. The solid lines have slopes of −1.1 for the fast system, −2.3 for the slow system with $\mu_0=0.9$, and −2.8 for the slow systems with $\mu_0=0.95$, 0.96 and 0.97. Units are described in footnote [30].

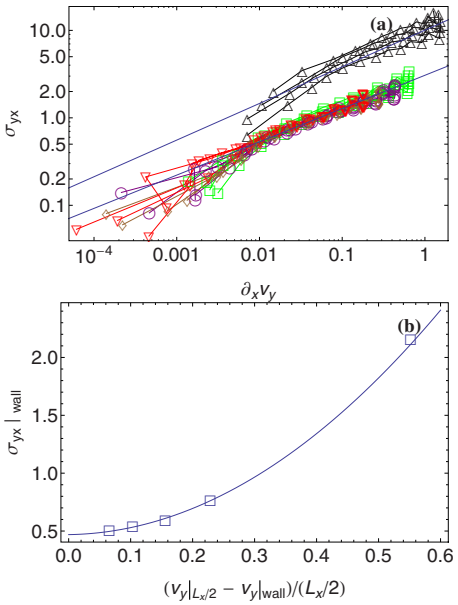

FIG. 9. (Color online) (a) Log-log plot of local shear stress σ_{yx} versus local shear rate $\partial_x v_y$ at a constant height in the glassy region for various flow rates (probability of reflection at the bottom sieve of $p=0.01$ as △'s, $p=0.1$ as □'s, $p=0.25$ as ○'s, $p=0.5$ as △'s, $p=0.75$ as ▽'s, and $p=0.9$ as ▲'s), all with an asymptotic coefficient of restitution of $\mu_0=0.9$. Lines connect data at fixed heights and each symbol is from a local measurement at a different x. The solid straight lines have slopes of 0.41 for the upper line and 0.38 for the lower line. (b) Plot of shear stress σ_{yx} at the wall versus the y velocity at the center at $L_x/2$ minus the y velocity at the wall, scaled by $L_x/2$. The yield stress σ_Y is indicated by the arrow. Data are from a $32\times32\times250$ column. Units are described in footnote [30].

cosity. That the viscosity is higher than the Enskog prediction at high density is not that surprising (this is also the case for elastic hard spheres although the difference is not as great), but at low density we see that the viscosity is much lower than would be predicted by the Enskog formula, a regime where elastic hard spheres show very close agreement with the Enskog prediction. This is probably due to the dissipation removing relative velocity of pairs of particles colliding along the x and z directions. At low density there are not enough collisions to randomize the particle velocities between collisions so very little mixing occurs in the x direction in the free-fall and free-fall/fluid transition regions [8], and hence very little transfer of momentum in the x direction (i.e., shear stress is suppressed relative to elastic hard sphere case).

Another interesting point is that in Figs. 7(b) and 7(c) we are plotting data from different simulations, with different coefficients of restitution, and, within the fluid region, all the data falls on the *same* curve whether we plot versus temperature or versus density (or ϕ). Thus, it would appear that, within the fluid regions, there must be a fairly well-defined relationship between density and temperature so we cannot distinguish the dependence on either variable within this region (i.e., in the chute flow geometry, T and ϕ are interchangeable within the fluid). Note that this is not generally true for an elastic hard sphere fluid where the density and temperature can be varied independently, as long as you constrain the volume of the system.

Numerous experiments have measured velocities and forces in sheared granular matter [1,48–50] confining granular matter in a Couette cell between a stationary outer cylinder and a rotating inner cylinder. These experiments are typically shearing a very dense granular state like our glass. In Ref. [51], the authors looked at the relationship between the square root of the granular temperature and shear rate that was observed in the glassy region of granular particles in a Couette cell. Our granular particles are in a shear flow traveling down the chute. The shear zones near the walls in the glassy state of our simulation should be comparable to these experiments. One might think that the shear zones along the walls in the glassy region are equivalent to a fluidized layer. As we shall see below, this does not turn out to be the case.

Following the analysis given in reference [51], using $\sigma_{xy}=\eta\dot{\gamma}$ with $\dot{\gamma}=\partial_x v_y$ being the shear rate and η the viscosity, an expression was made for the viscosity to scale with the collision frequency,

$$\eta \sim P/(\rho_c d^2 T^{1/2}), \tag{44}$$

where d is the particle diameter, η_0 is a dimensionless number, and $\rho\sim\rho_c$ the close-packed density has been assumed, so that

$$T^{1/2} \sim P/(\rho_c d^2 \sigma_{xy})\dot{\gamma}. \tag{45}$$

However, this analysis can be taken further. If the pressure given in Eq. (44) followed the scaling $P \sim \rho T$, this would give the same scaling $\eta \sim T^{1/2}$ as Eq. (42) for a hard sphere gas. This extension was not done in Ref. [51]. The analysis that was provided by the authors in Ref. [51], resulting in Eq. (45), gives $\dot{\gamma}=\partial_x v_y \sim T^{1/2}$. Their analysis did not lead to agreement with their experiment. Experimentally, they observed the following power law with

$$T^{1/2} \sim |\partial_x v_y|^{0.4}. \tag{46}$$

A log-log plot of the square root of the granular temperature vs shear rate as measured from our simulation on one side of the chute (from middle to the wall) in the glassy region is shown in Fig. 8(a). Again, each line is at a fixed height and each point is from a different value of x at that height where the temperature and strain rate are locally measured. We plotted this for a series of systems with different probabilities of sieve reflection, p and different asymptotic coefficients of restitution μ_0. On a log-log plot the top curve in Fig. 8(a) vaguely resembles a power-law exponent of 0.4 as in experiment [51] for a fast system ($p=1\%$, $\mu_0=0.9$), and as shown by the superimposed bottom curves in Fig. 8(a), for the slower systems ($p=90\%$) with $\mu_0=0.9$, 0.95, 0.96 and 0.97, the slope is 0.2, although this is not as clear a linear regime on a log-log plot of the square root of the granular temperature (velocity fluctuations) vs the shear rate for the slower systems as for the faster system. Thus the power-law exponent of 0.4 that was reported in the experimental paper [51] is not universal.

Equation (46) indirectly assumes that the viscosity in the sheared glass is a function of the granular temperature. Using the relation $\sigma_{xy}=\eta\partial_x v_y$, we can plot the viscosity, η as $\sigma_{xy}/\partial_x v_y$, versus the granular temperature, T, in the glassy region for both a slow ($p=90\%$) system yielding a power law of 1.1 and a fast ($p=1\%$) system yielding a power law of 2.3. This is shown as a log-log plot in Fig. 8(b). Clearly, the power-law exponent is not universal here. Thus, the evidence strongly suggests that the sheared glass is *not* simply equivalent to a liquefied boundary layer near the walls (otherwise it would behave as in Fig. 7 where the viscosity from different simulations fell on the same curve as a function of T or ϕ).

We can however obtain a universal power law in the sheared glass by plotting the shear stress, σ_{xy}, vs. the shear rate, $\partial_x v_y$, on a log-log plot as shown in Fig. 9(a). Again, each line is at a fixed height and each point is from a different value of x at that height where the shear stress and strain rate are locally measured. We found a universal power law of 0.39 ± 0.02 for both slow and fast systems on one side of the chute,

$$\sigma_{xy} = B|\partial_x v_y|^{0.39}, \tag{47}$$

with B a constant. This is equivalent to obtaining a universal power law by further plotting (not shown) the viscosity, η on one side of the chute in the glassy region versus the shear rate, $\dot{\gamma}=\partial_x v_y$ and witness a universal power law of approximately -0.6:

$$\eta = B|\partial_x v_y|^{-0.6} \tag{48}$$

While there is a clear power law in Fig. 9(a), it is also clear that there is a dependence on other variables as the curves do not all overlap. We will come back to this point in Sec. II H.

The universal power-law between the shear stress and strain rate given by Eq. (47) and shown in Fig. 9(a) makes one wonder whether we have a true glassy region. Consider in Fig. 9(a) a typical region where a particle of radius a undergoes a strain rate $\partial_x v_y$ of 0.01. In this region, $v_y \sim 1$ so using the relation

$$\partial_x v_y = \frac{\Delta v}{a}, \tag{49}$$

we can say that it takes 100 time units for one grain to pass another. However, using the typical size and velocities from Fig. 1 the time that a particle has in the glassy portion of the chute is

$$\frac{L_y}{v_y} \approx \frac{200}{1} = 200 \text{ time units}. \tag{50}$$

Thus, in our glassy region, it takes about the same amount of time for one grain to pass another as it takes for all the particles to traverse the entire chute. It is also clear from Fig. 9(a) that Eq. (47) is not valid all the way into the interior (low strain-rate region) of the system and significant deviations occur below $\sigma_{xy} \lesssim 0.4$. Another significant caveat is that we have taken the strain rate $\partial_x v_y$ as the derivative of the *time*-averaged velocity profile. While the time-averaged profile is smooth, an instantaneous velocity profile is much more discontinuous (so much so that one cannot meaningfully take a numerical derivative) suggesting more discrete faultlike slips occurring in the glass rather than the local rearrangements typical of a fluid.

If we look at the plot of shear stress at the wall (experimentally measurable shear stress) versus the scaled y velocity at the center minus the y velocity at the wall (experimentally observable strain rate) shown in Fig. 9(b), we do observe a finite shear stress when the scaled y velocity at the center minus the y velocity at the wall is zero. This indicates that our glassy region has a yield stress at this zero velocity as would be expected for a glassy region. Doing the same thing in the fluid region (not shown) shows a 0 intercept at small strain rates indicating the lack of a yield stress there. A constitutive relation for the static central portion of the glass is still needed as we have only really described the shear zones near the wall in this section. We will consider this in more detail in Sec. II H.

It is interesting to note that in no region do we observe the Bagnold scaling [1] of

$$\sigma_{xy} \sim (\partial_x v_y)^2. \tag{51}$$

However, Bagnold did not measure the shear stress or strain rate locally but rather deduced them from the externally applied stress and strain in a Couette cell. This is more similar to our analysis in Fig. 9(b) which does exhibit this quadratic relationship. However, our simulation is more akin to Poiseuille flow rather than Couette flow so a direct comparison is not necessarily valid. However, it does raise the possibility

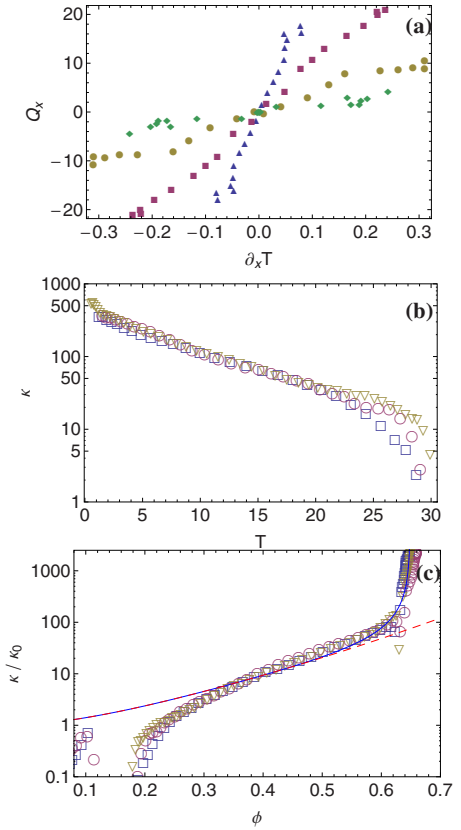

FIG. 10. (Color online) (a) Heat flux Q_x versus granular temperature gradient, $-\partial_x T$, in the fluid region (probability of reflection at the bottom sieve of p=90%, μ_0=0.97). Data points with the same symbol shape were measured at the same height but different x in the fluid regions (▲'s at y=274, ■'s at y=284, ●'s at y=294 and ◆'s at y=304). (b) Semilogarithmic plot of thermal conductivity, $\kappa=-Q_x/\partial_x T$ versus the granular temperature, T, in the fluid region for systems with a probability of reflection at the bottom sieve of p=90%. The symbols indicate different asymptotic coefficients of restitution, μ_0 (with □'s using μ_0=0.95, ○'s using μ_0=0.96, and ▽'s using μ_0=0.97). (c) Same data as in (b) but scaled by κ_0 [Eq. (57)] and plotted versus volume fraction ϕ. The lines are from an Enskog prediction described in the text. Units are described in footnote [30].

that Bagnold scaling is, similar to the relationship between δv and v found by Menon and Durian [6,8], not a local relationship but a statement about a more global force/energy balance. However, simulations in the Couette geometry would be needed to comment further on this aspect. Simulations using Hertzian contact types of interactions have seen regions of Bagnold scaling [52]. However, these simulations found that in the regions where Bagnold scaling was observed transmission of stresses was dominated by contacts rather than collisions. It is possible that the addition of tangential dissipation (i.e. friction) during a collision would be key to seeing Bagnold scaling but, if so, would not be consistent with Bagnolds original argument which was based on binary collisions.

G. Energy equation

In Sec. II A, the energy conservation during steady-state was expressed as

$$\partial_t(E) + \partial_\alpha(F_\alpha) = I + \rho g \cdot \mathbf{v}. \tag{52}$$

In this section, we will examine the energy flux $\mathbf{F}$ and the dissipation I and relate them to the density and temperature. We assume that the time derivative, $\partial_t E$ is zero because we are in steady state. We will focus first on the energy flux $\mathbf{F}$.

As stated in [32], there is a difference between the "energy flux," $\mathbf{F}$, and the "heat flux," $\mathbf{Q}$. The heat flux, $\mathbf{Q}$ is the uncorrelated part of the energy flux, and can be found using

$$\mathbf{Q} = \mathbf{F_c} + (\boldsymbol{\sigma} \cdot \mathbf{v}), \tag{53}$$

where $\mathbf{F_c}$ is the collision energy flux defined by Eq. (10) and $\boldsymbol{\sigma}$ is the stress tensor defined by Eq. (5). In Eq. (53), $\boldsymbol{\sigma}\cdot\mathbf{v}$ represents the *coherent* transfer of energy (i.e., nondissipative) during collisions.

Fourier's law suggests that the heat flux across the chute, Q_x, can be expressed as proportional to the gradient of the granular temperature, T, by the relation

$$Q_x = -\kappa \partial_x T, \tag{54}$$

where κ is the thermal conductivity. In our *fluid* region, we plotted the heat flux, Q_x versus the gradient of the granular temperature, $\partial_x T$, across the width (x direction) of the chute. This is shown in Fig. 10(a) for a slow system using a probability of reflection at the bottom sieve of p=90% and an asymptotic coefficient of restitution of μ_0=0.95. Again, each line (set of points with the same symbol shape) is at a fixed height and each point is from a different value of x at that height where the heat flux and temperature gradient are locally measured. Systems with higher coefficients of restitution had the largest fluid regions. It was important here to choose a system with a high asymptotic coefficient of restitution in order to maintain a true fluid region. Otherwise with lower coefficients of restitution, we would have just a combination of fluid to glass and fluid to free-fall transition regions. As one can see for various heights in the fluid region, the data in Fig. 10(a) fall on straight lines. The negative slopes of these straight lines give the thermal conductivity

$$\kappa = -\frac{Q_x}{\partial_x T}. \tag{55}$$

In Fig. 10, the thermal conductivity, κ was calculated as a linear fit and is shown on a semilogarithmic plot versus the granular temperature at a range of heights in the fluid region for three slow systems (p=90%). Fig. 10 shows systems with different asymptotic coefficients of restitution of μ_0=0.95 shown as □'s, 0.96 shown as ○'s and 0.97 shown as ▽'s. Interestingly, all three systems consistently give an exponential fit in the fluid region of

$$\kappa = Ae^{-T/T_0}, \tag{56}$$

where $T_0 \sim 8.4$, and A is a multiplicative constant.

We can contrast Eq. (56) to a thermal conduction expression for a hard sphere gas given in Ref. [46]

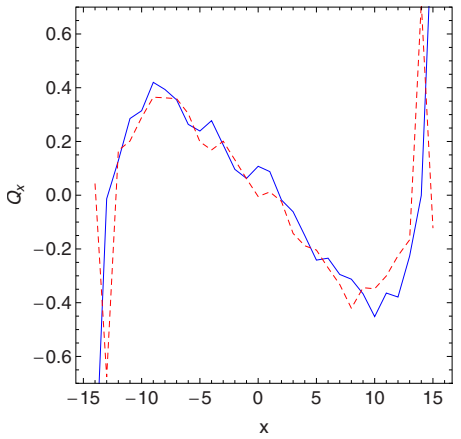

FIG. 11. (Color online) Log-log plot of heat flux $Q_x=-\kappa\partial_x 3T$ vs width x for a 15% polydisperse 3D simulation for a glassy region at $y=200$ where $\kappa=4/3\pi a^3\rho f_c$. The solid line is $Q_x=F_{cx}+\sigma_{xy}v_y$, and the dashed line is $Q_x=-4/3\pi\langle a^3\rangle\rho f_c\partial_x 3T$. Units are described in footnote [30].

$$\kappa_0 = \frac{125}{384}\frac{1}{a^2}\left(\frac{T}{\pi m}\right)^{1/2}. \tag{57}$$

From the equation for the thermal conductivity of a hard sphere gas given by Eq. (57), one gets the impression that $\kappa\sim T^{1/2}$ and thus that the thermal conductivity should increase with temperature. The thermal conductivity for our granular fluid does not increase with temperature, but exponentially decays with increasing temperature as given by Eq. (56). Thus once again our granular fluid cannot be considered as a hard sphere gas. Our fluid behaves as a liquid: as the temperature goes down, the thermal conductivity increases as you would expect in a material that approaches a solid state as our glassy region. Just as there is an Enskog prediction for the viscosity, there is an Enskog prediction for the thermal conductivity of an elastic hard sphere fluid at higher densities [47]

$$\frac{\kappa}{\kappa_0} = 4\phi\left(\frac{1}{Z}+1.2+0.757Z\right), \tag{58}$$

with Z having the same meaning as in Eq. (43). The Enskog prediction is plotted, along with the data from the simulation, in Fig. 10(c). Once again, the agreement at low density is very poor, probably for the same reasons discussed for the viscosity. However, at higher densities, the expression is not unreasonable.

Next, we examine the thermal conductivity in the *glassy* region. The heat flux, Q_x is plotted in the glassy region in Fig. 11 across the width (x direction) of the chute. As shown in Fig. 11, in the glassy region

$$\kappa = 3\phi f_c = \frac{4}{3}\pi\langle a^3\rangle\rho 3 f_c, \tag{59}$$

(the density times the collision frequency). Equation (59) is the same equation as in Ref. [32] found in 2D where we measured density there as a volume fraction [53]. As the collision frequency is known in terms of the density and

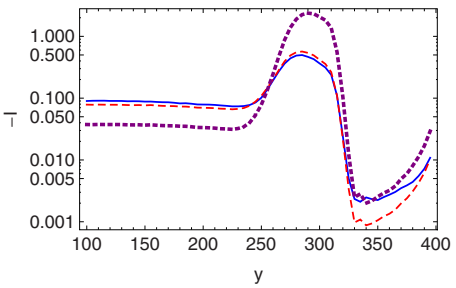

FIG. 12. (Color online) Semilogarithmic plot of the negative of the dissipation, $-I$, from the simulation as calculated from Eq. (11) (blue solid line), as calculated using Eq. (63) (red dashed line), and as calculated using Eq. (64) (purple dotted line). Units are described in footnote [30].

temperature (Sec. II D) this gives a closed expression for the conductivity in the glass.

The remaining term for which we need a constitutive relation is the dissipation, I. Since the coefficient of restitution μ, is highly correlated with the impact velocity v_n, we cannot simply factor the terms in Eq. (11), $-\frac{1}{4}\langle(1-\mu^2)v_n^2\rangle$ as $-\frac{1}{4}\langle 1-\mu^2\rangle\langle v_n^2\rangle$ [we could factor out $(1+\mu)$ in previous expressions, such as for the collision frequency, because the *relative* change in $(1+\mu)$ for different v_n is small whereas the relative change in $(1-\mu^2)$ for different v_n is large]. We outline below two different constitutive relations for I based on different assumptions.

In the first case, we assume that dissipation is dominated by the high impact collisions. We consider a small proportion, say b, of the dissipation involves v_n being greater than the cutoff velocity v_0 in our velocity-dependent coefficient of restitution Eq. (2), and a proportion $1-b$ of the dissipation involves $v_n<v_0$. Then we have

$$\begin{aligned}\langle \delta I\rangle &= \left\langle -\frac{1}{4}(1-\mu^2)v_n^2\right\rangle \\ &= b\left\langle -\frac{1}{4}(1-\mu_0^2)v_n^2\right\rangle_{v_n>v_0} \\ &\quad + (1-b)\left\langle -\frac{1}{4}(1-\mu^2)v_n^2\right\rangle_{v_n<v_0}.\end{aligned} \tag{60}$$

Now, for $v_n<v_0$

$$\left\langle -\frac{1}{4}(1-\mu^2)v_n^2\right\rangle_{v_n<v_0} \approx 0, \tag{61}$$

because $\mu\approx 1$ and v_n is also small for these collisions. Similarly, the small value of v_n for collisions with $v_n<v_0$ gives

$$\begin{aligned}\langle v_n^2\rangle_{\mathbf{all}} &= b\langle v_n^2\rangle_{v_n>v_0} + (1-b)\langle v_n^2\rangle_{v_n<v_0}, \\ &\approx b\langle v_n^2\rangle_{v_n>v_0}.\end{aligned} \tag{62}$$

Putting it all together gives

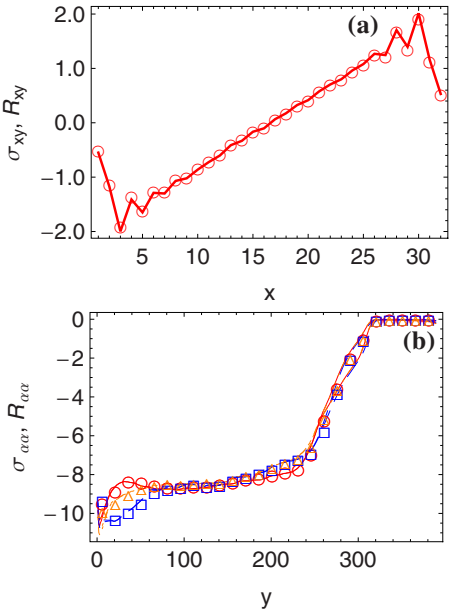

FIG. 13. (Color online) Shear stress σ_{xy} (solid line) and R_{xy} (circles) [right hand side of Eq. (66)], the shear stress factorized into the collision directions, $\langle(\hat{\mathbf{q}}\cdot\hat{\mathbf{x}})(\hat{\mathbf{q}}\cdot\hat{\mathbf{y}})\rangle$ and the constant $-\frac{1}{2}f_c\langle(1+\mu)(\dot{\mathbf{r}}_1-\dot{\mathbf{r}}_2)\cdot\hat{\mathbf{q}}\rangle$ versus x in (a) the glassy region at a height, $y=100$. (b) Plot of the diagonal stress, $\sigma_{\alpha\alpha}$ with its kinetic term (lower curves) and without its kinetic term (upper curves), and factor $R_{\alpha\alpha}$ versus height y. (σ_{xx} is the solid line, σ_{yy} is the dashed line, and σ_{zz} is the dot-dashed line, R_{xx} is circles, R_{yy} is squares, and R_{zz} is triangles). Data are for a 400-height column using an asymptotic coefficient of restitution μ_0 of 0.97 and a probability of reflection, $p=0.9$. Units are described in footnote [30].

$$\langle \delta I\rangle = \frac{1}{4}(1-\mu_0^2)\langle v_n^2\rangle. \tag{63}$$

This is the expression we expect to be correct if high velocity impacts dominate the dissipation.

However, most collisions occur with $v_n < v_0$ (although these collisions are less dissipative so they may, or may not, impact the total dissipation I). If the coefficient of restitution formula for $v_n < v_0$ is used directly and substituted into Eq. (2) and the average of the entire expression is evaluated one gets

$$\langle \delta I\rangle = \frac{1}{2}\frac{(1-\mu_0)}{v_0^{0.7}}\langle v_n^{2.7}\rangle - \frac{(1-\mu_0)^2}{4v_0^{1.4}}\langle v_n^{3.4}\rangle. \tag{64}$$

One can relate the averages of $\langle v_n^{2.7}\rangle$ and $\langle v_n^{3.4}\rangle$ to $\langle v_n^2\rangle$ similar to Eq. (29). The total dissipation can be found as

$$I = \langle \delta I\rangle f_c, \tag{65}$$

with f_c given in terms of density and temperature as described in Sec. II D.

Figure 12 shows, on a semilogarithmic plot, the dissipation from the simulation plotted along with the constitutive Eqs. (63) and (64) (multiplied by the collision frequency). The constitutive equation given by Eq. (63) matches the dissipation from the simulation nicely in the liquid and glass regions, strongly supporting the argument that dissipation in these regions is completely dominated by the high impact velocity collisions. For the free-fall region the dissipation goes from Eq. (64) at the top to Eq. (63) at the fluid-free-fall transition. Thus, somewhat surprisingly the free-fall region is the only region where the dissipation is not dominated by the higher velocity collisions.

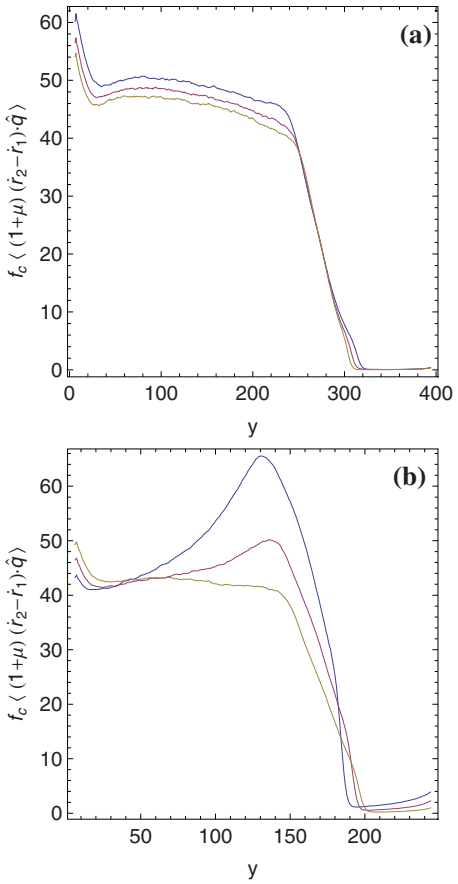

FIG. 14. (Color online) (a) Plot of $f_c\langle(1+\mu)(\dot{\mathbf{r}}_1-\dot{\mathbf{r}}_2)\cdot\hat{\mathbf{q}}\rangle$ vs height y for a 400-height column. The lines from bottom to top represent data with asymptotic coefficients of restitution μ_0 of 0.95, 0.96, and 0.97, all with a sieve reflection probability, $p=0.9$. Data are averaged over the width (x direction). (b) Plot of $f_c\langle(1+\mu)(\dot{\mathbf{r}}_1-\dot{\mathbf{r}}_2)\cdot\hat{\mathbf{q}}\rangle$ vs height y for a 250-height column. The lines from top to bottom represent data with sieve reflection probabilities p of 0.25, 0.5, and 0.75, all with an asymptotic coefficient of restitution $\mu_0=0.9$. Units are described in footnote [30].

H. Static limit

We now examine the existence of a static limit to the glassy state of our system. The relationship between stress and strain rate in the glassy region, Eq. (47), is not that satisfying as one approaches the static limit because it is really a time-averaged response function. That is, as mentioned in Sec II F, for the low strain rates near the center of the chute it may take more time on average for one grain to pass another than it takes all particles to traverse the entire chute. As one approaches the static limit the time one would need to average over for this to be a useful constitutive relation becomes longer and longer. In this section we examine

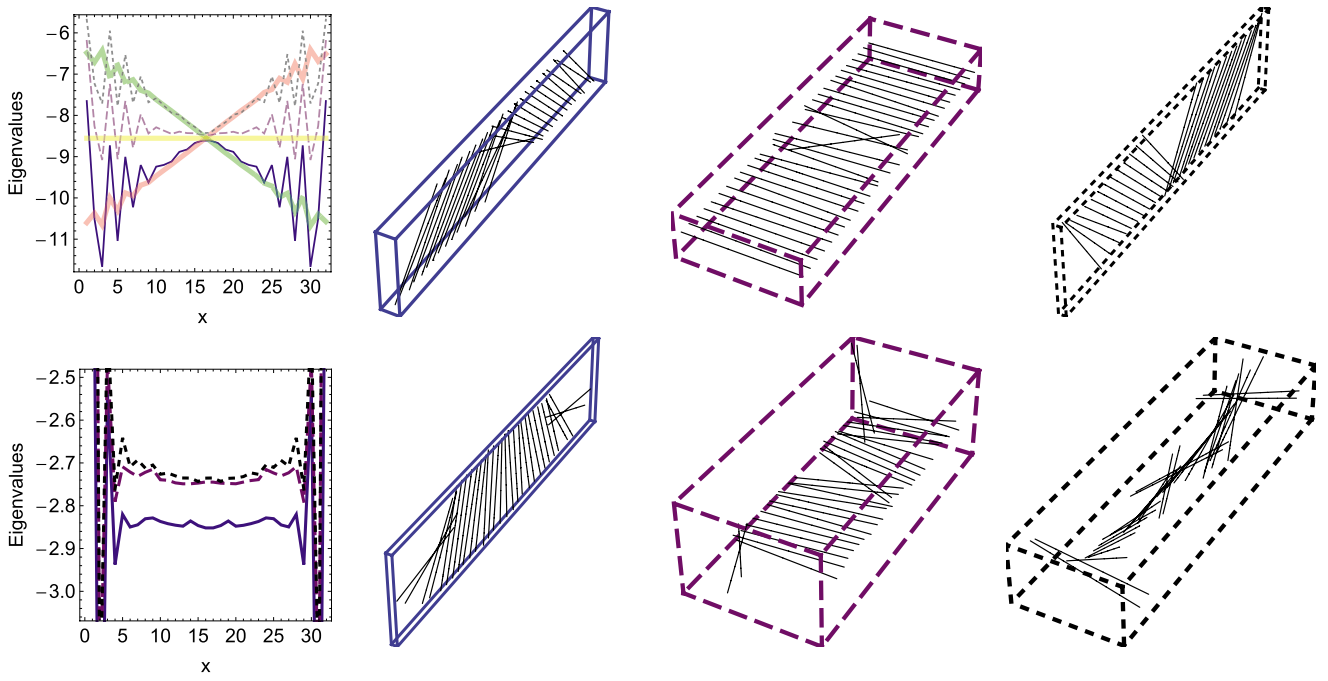

FIG. 15. (Color online) Plot of the eigenvalues (compressive stresses) and corresponding directions of the stress tensor along width of column in (top) the glassy region at $y=138$, and (bottom) in the fluid region at $y=294$ for a 400-height column using an asymptotic coefficient of restitution μ_0 of 0.97. In both (top) and (bottom), the eigenvalues are associated alongside with the eigenvector directions by the style of the lines. That is, the line style of the eigenvalues (shown as solid, dashed, or dotted lines) are matched with the line style of the box (shown as a solid, dashed, or dotted lined box) surrounding the particular eigenvector directions. The analytical solution for the eigenvalues given by Eq. (74) with $c=0$ is plotted as thick lines with Λ_1 drawn in pink, Λ_2 in green and Λ_3 in yellow. Units are described in footnote [30].

the stress in the glassy region in more detail and relate it to various other constitutive relations proposed for static granular materials. First we will demonstrate that there is a static limit to our equations for stress.

In the first step to simplifying the stress tensor, we write the 3D stress tensor given in Eq. (6) as [32]

$$\sigma_{\alpha\beta} \approx -\langle \rho(v_\alpha - \langle v_\alpha \rangle)(v_\beta - \langle v_\beta \rangle)\rangle - \frac{1}{2} f_c \langle (1+\mu)(\dot{\mathbf{r}}_1 - \dot{\mathbf{r}}_2)\cdot\hat{\mathbf{q}}\rangle \times \langle (\hat{\mathbf{q}}\cdot\hat{\mathbf{e}}_\alpha)(\hat{\mathbf{q}}\cdot\hat{\mathbf{e}}_\beta)\rangle \tag{66}$$

In Eqs. (5) and (66) the sum is over collisions in a (long) time interval t and f_c is the collision frequency. In going from Eq. (5)–(66) we have assumed that we could separate the factor $(1+\mu)(\dot{\mathbf{r}}_1-\dot{\mathbf{r}}_2)\cdot\hat{\mathbf{q}}$ from the factors in the matrix $\langle(\hat{\mathbf{q}}\cdot\hat{\mathbf{e}}_\alpha)(\hat{\mathbf{q}}\cdot\hat{\mathbf{e}}_\beta)\rangle$ when computing averages (i.e., we have assumed that these factors are statistically independent). The validity of this assumption is shown in Fig. 13 which plots the stress components $\sigma_{\alpha\beta}$ directly from Eq. (5) where the terms are unfactored, and $R_{\alpha\beta}=\frac{1}{2}f_c\langle(1+\mu)(\dot{\mathbf{r}}_1-\dot{\mathbf{r}}_2)\cdot\hat{\mathbf{q}}\rangle\times\langle(\hat{\mathbf{q}}\cdot\hat{\mathbf{e}}_\alpha)(\hat{\mathbf{q}}\cdot\hat{\mathbf{e}}_\beta)\rangle$ versus the width x or height y. As advertised, the virial term factors.

In a granular glass the kinetic term, $\langle \rho v_\alpha v_\beta\rangle$ is negligible. As shown in Fig. 14(a), the factor $f_c\langle(1+\mu)(\dot{\mathbf{r}}_1-\dot{\mathbf{r}}_2)\cdot\hat{\mathbf{q}}\rangle$ in front of the matrix changes dramatically in the fluid region but in comparison appears to be nearly constant in the glassy region. Fig. 14(b) plots the factor $f_c\langle(1+\mu)(\dot{\mathbf{r}}_1-\dot{\mathbf{r}}_2)\cdot\hat{\mathbf{q}}\rangle$ for different sieve reflection probabilities and shows that for slower systems, this factor approaches a constant. Hence the structure of the stress tensor in the glass comes almost entirely from the collision directions [i.e., the $\langle(\hat{\mathbf{q}}\cdot\hat{\mathbf{e}}_\alpha)(\hat{\mathbf{q}}\cdot\hat{\mathbf{e}}_\beta)\rangle$ terms in Eq. (66)]. This is very reminiscent of models describing static granular materials based on force chains.

For our particular case, we do not actually need a further relation for the shear stress to solve the stress balance Eq. (12). As $\partial_y\sigma_{yy}\approx 0$ in the glassy state, it is clear that $\sigma_{xy}\approx\rho g x+$constant. Making use of symmetry about the center ($x=16$) of the chute, it follows that the constant should be $-\rho g 16$. However, this is really just a statement about stress balance in the system and requires the *a priori* assumption of the shear stress supporting the weight. In order to compare to other constitutive relations suggested for static granular materials it is worthwhile to decompose the stress/pressure tensor into its eigenvalues Λ_i and eigenvectors $\hat{\boldsymbol{n}}$, $\hat{\boldsymbol{m}}$, and $\hat{\boldsymbol{l}}$:

$$p_{\alpha\beta} = -\sigma_{\alpha\beta} = \Lambda_1 n_\alpha n_\beta + \Lambda_2 m_\alpha m_\beta + \Lambda_3 l_\alpha l_\beta. \tag{67}$$

Note that the stress tensor is real, symmetric, and nonsingular so the eigenvectors are mutually orthogonal. The measured values of the eigenvalues and eigenvectors of our stress tensor are shown in Fig. 15. Note that the tensor nature of the stress is determined entirely by $\langle(\hat{\mathbf{q}}\cdot\hat{\mathbf{e}}_\alpha)(\hat{\mathbf{q}}\cdot\hat{\mathbf{e}}_\beta)\rangle$ so eigenvectors tell us about the directions of the *collision chains* in our system (as $\hat{\mathbf{q}}$ are the directions of the collisions) and these typically propagate through our particles at 45° to the x/y axes as seen in Fig. 15: in the glassy region of our system these "directors" can be expressed as

$$\hat{\boldsymbol{n}} = \left(\frac{1}{\sqrt{2}}, \frac{1}{\sqrt{2}}, 0\right), \tag{68a}$$

$$\hat{\boldsymbol{m}} = \left(-\frac{1}{\sqrt{2}}, \frac{1}{\sqrt{2}}, 0\right), \tag{68b}$$

$$\hat{\boldsymbol{l}} = (0,0,1). \tag{68c}$$

This connection of the eigenvectors of the stress tensor with collision chains is very similar to models proposed for static sandpiles, such as the fixed principle axes (FPA) models [14]. These early models suggested "$\hat{\boldsymbol{n}}$, $\hat{\boldsymbol{m}}$, $\hat{\boldsymbol{l}}$ (as) directors along three nonparallel populations of force chains; the Λ's are compressive pressures acting along these. Body forces cause $\Lambda_{1,2,3}$ to vary in space," [14], however $\hat{\boldsymbol{n}}$, $\hat{\boldsymbol{m}}$, $\hat{\boldsymbol{l}}$ are fixed and are not allowed to change in space, at least in some of these models. They must be determined from global symmetries and boundary conditions.

We can, however, solve for the eigenvalues and eigenvectors of the stress tensor independent of any particular model. *Any* stress tensor of the expected form,

$$\begin{pmatrix} -p & \tau & 0 \\ \tau & -p & 0 \\ 0 & 0 & -p \end{pmatrix} \tag{69}$$

has the eigenvectors of Eq. (68). Using Eqs. (4) and (12) in the static limit, we have component wise

$$\partial_x \sigma_{yx} + \partial_y \sigma_{yy} = -\rho g_y = \rho g, \tag{70a}$$

$$\partial_x \sigma_{xx} + \partial_y \sigma_{xy} = 0, \tag{70b}$$

$$\partial_z \sigma_{zz} = 0. \tag{70c}$$

Using the known stress directors Eqs. (68) we can express the stress tensor in terms of its eigenvalues in our glassy region giving

$$\sigma_{xy} = \sigma_{yx} = -\Lambda_1 \frac{1}{2} + \Lambda_2 \frac{1}{2}, \tag{71a}$$

$$\sigma_{yy} = -\Lambda_1 \frac{1}{2} - \Lambda_2 \frac{1}{2}, \tag{71b}$$

$$\sigma_{xx} = -\Lambda_1 \frac{1}{2} - \Lambda_2 \frac{1}{2}, \tag{71c}$$

$$\sigma_{zz} = -\Lambda_3. \tag{71d}$$

Finally, combining Eqs. (70) and (71) we arrive at

$$(\partial_x \Lambda_1 - \partial_x \Lambda_2)\frac{1}{2} + \frac{1}{2}(\partial_y \Lambda_1 + \partial_y \Lambda_2) = -\rho g, \tag{72a}$$

$$(\partial_x \Lambda_1 + \partial_x \Lambda_2)\frac{1}{2} + \frac{1}{2}(\partial_y \Lambda_1 - \partial_y \Lambda_2) = 0, \tag{72b}$$

$$\partial_z \Lambda_3 = 0. \tag{72c}$$

The general solution to Eqs. (72) is

$$\Lambda_1 = -\rho g x + C_1(y - x),$$

$$\Lambda_2 = \rho g x + C_2(x + y),$$

$$\Lambda_3 = C_3(x,y), \tag{73}$$

where C_1, C_2, and C_3 are arbitrary functions of the arguments indicated. Thus, we see that just specifying the eigenvectors, as in FPA models, still does not leave us with a solution without arbitrary functions. Even the boundary conditions do not uniquely specify a solution as different solutions are possible in different regions. If we invoke symmetry properties at midwidth (at $x=16$) then

$$\Lambda_1 = -(\rho g - c)(x - 16) - cy + p,$$

$$\Lambda_2 = (\rho g - c)(x - 16) - cy + p,$$

$$\Lambda_3 = -cy + p, \tag{74}$$

is the most general solution if we restrict ourselves to linear functions for the C_i. Taking $c \approx 0$ gives a good match to the observed eigenvalue solutions in the glassy region plotted as thick transparent lines in the top left plot of Fig. 15. These lines reasonably match our simulation data. Taking $c = \rho g$ gives the hydrostatic case (isotropic everywhere, weight supported by a pressure gradient) which would result in our stress tensor having no shear stresses, a situation much closer to that observed in the fluid where shear stresses are much smaller than in the glassy region. If the fluid were perfectly isotropic we could get linear combinations of eigenvectors for degenerate eigenvalues. However, this isotropy is broken in the y direction and so the eigenvectors in the fluid region are not exactly those of Eq. (68) and the near degeneracy leads to more noise, especially near the boundaries. As we know the glassy region is supported by shear stress and the liquid by a pressure gradient we can distinguish limiting cases in our system but cannot determine *c a priori*.

A more recently proposed constitutive law for dense granular flows [54] is that the effective viscosity

$$\eta = \chi P / \sqrt{0.5 \partial_\alpha v_\beta \partial_\alpha v_\beta}, \tag{75}$$

where χ is an internal friction coefficient. In our case, this implies that

$$\sigma_{xy} = \sqrt{2} \chi P. \tag{76}$$

In the dense glassy region of our system, we have established that the thermal contribution to the stress tensor is negligible so that Eq. (66) becomes

$$\sigma_{\alpha\beta} \approx -\frac{1}{2} f_c \langle (1+\mu)(\dot{\mathbf{r}}_1 - \dot{\mathbf{r}}_2) \cdot \hat{\mathbf{q}} \rangle \langle (\hat{\mathbf{q}} \cdot \hat{\mathbf{e}}_\alpha)(\hat{\mathbf{q}} \cdot \hat{\mathbf{e}}_\beta) \rangle$$

$$= \langle (\hat{\mathbf{q}} \cdot \hat{\mathbf{e}}_\alpha)(\hat{\mathbf{q}} \cdot \hat{\mathbf{e}}_\beta) \rangle P, \tag{77}$$

where we have used the relation $P = -\frac{1}{3} Tr\, \sigma_{\alpha\beta}$ and that $Tr \langle (\hat{\mathbf{q}} \cdot \hat{\mathbf{e}}_\alpha)(\hat{\mathbf{q}} \cdot \hat{\mathbf{e}}_\beta) \rangle \equiv 1$ as $\hat{\mathbf{q}}$ is a unit vector. Thus we see that

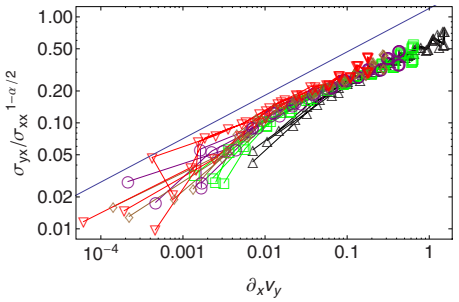

FIG. 16. (Color online) Shear stress σ_{xy} scaled by pressure σ_{xx} raised to the $1-\alpha/2$, with $\alpha=0.39$ for *all* of the data plotted in Fig. 9(a). Again, each symbol is at a different x along a cross section going from the wall into the center of the chute and lines connect data at a common height (and pressure).

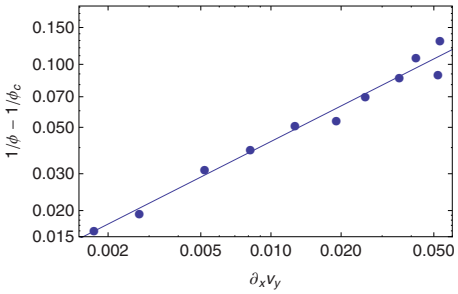

FIG. 17. (Color online) Inverse of the volume fraction ϕ in the glass (height of $y=125$) versus the strain rate $\partial_x v_y$ (each symbol is at a different x along a cross section going from the wall into center of the chute) using an asymptotic coefficient of restitution μ_0 of 0.97. Units are described in footnote [30].

Eq. (76) appears to comes out naturally as *all* components of the stress tensor are proportional to P, as long as the thermal contribution to the stress is negligible. Thus, the so-called friction coefficient χ is just the correlation in collision directions $\langle \hat{q}_x \hat{q}_y \rangle$ in the microscopic picture. For simple shear flows, Ref. [54] also found that the relation

$$\chi = \chi_s + \chi_2(\dot{\gamma}, P), \tag{78}$$

worked well, where the first term χ_s is a constant and the second term is a function of shear rate and pressure and vanishes in the limit that $\dot{\gamma} \to 0$. The specific functional form for χ_2 suggested by Ref. [54] is not a good fit to our observations in Sec. II F, in particular Eq. (47) and Figure 9(a). However, the form suggested by Ref. [54] was used for grains with friction. Peyneau and Roux [31] found that their simulations of homogeneously sheared *frictionless* grains gave a slightly different form and was fit well by

$$\sigma_{xy} = [\chi_s + c(\partial_x v_y/\sqrt{P})^{\alpha}]P \tag{79}$$

with c a constant, and they found $\alpha \approx 0.39$. A direct fit to this expression for our data in the glassy region gives $\chi_s=0$ and $\alpha=0.39$ [again local measurement of σ_{xy}, $\partial_x v_y$, and P along points at different x going from the center of the column to the wall, as in Figure 9(a)]. Thus we have excellent agreement for the exponent, but for their homogeneously sheared system they found $\chi_s \neq 0$. Note that the pressure is effectively independent of x, as should be evident from Eq. (74) and the fact that $P=(\Lambda_1+\Lambda_2+\Lambda_3)/3$. This and the fact that our fit gives $\chi_s=0$, leads us to see that Eq. (79) is equivalent to the form, including the *identical* exponent, we fit in Sec. II F, Eq. (47) with $B=cP^{1-\alpha/2}$. The result is shown in Fig. 16. Comparing this figure to Fig. 9(a), we see that the addition of the local pressure dependence results in a much improved collapse of the data onto a single curve. Adding a particle mass density dependence to Eq. (79) as might be expected if χ were strictly a function of R_I (see introduction) did not improve the collapse.

It is important to note the different interpretation of the constitutive relation Eq. (76) and the microscopic relation Eq. (77) in the case where the strain rate vanishes. The constitutive relation Eq. (76) is to be interpreted as: if $\sigma_{xy}/P \leq \chi_s$ then $\partial_x v_y=0$. It does *not* say that $\sigma_{xy}=\chi_s P$ in this case. However, the microscopic stress relation Eq. (77) tells us that σ_{xy} and P are *still* proportional in this case ($\sigma_{xy}/P \leq \chi_s$) but $\langle(\hat{\mathbf{q}}\cdot\hat{\mathbf{e}}_\alpha)(\hat{\mathbf{q}}\cdot\hat{\mathbf{e}}_\beta)\rangle$ may, or may not, be constant.

Peyneau and Roux [31] also found a shear induced dilation that they fit to

$$\phi^{-1} = \phi_c^{-1} + D(\partial_x v_y/\sqrt{P})^{\nu}, \tag{80}$$

with D a constant and $\nu \approx 0.41$. We find a similar dilation in the glass going from the center of the chute (where the shear rate is zero) to the wall, as shown in Fig. 17. Here all the points are at a fixed height and each point is from a different value of x at that height where the volume fraction and strain rate are locally measured. However, we find an exponent of $\nu \approx 0.6$. Considering Peyneau and Roux were using a homogeneous shearing and a Hertzian contact model whereas we have the additional layering of grains in the shear zones near the walls (due to the flat walls) and hard spheres, the agreement is still reasonable. This suggests that the results we have found are fairly robust to the details of the model.

III. CONCLUSION

In this paper we investigated constitutive relations in the free-fall, fluid, and glassy states observed in our simulations of granular matter. The pressure in all regions of the system was well described by what would be expected of a elastic hard sphere gas. However, the transport coefficients were distinctly different from what one would expect from kinetic theory. The viscosity and thermal conductivity increases with decreasing temperature in the fluid state, apparently diverging in the $T \to 0$ limit. The thermal conductivity and dissipation were found in terms of the density, temperature and average collision frequency. The collision frequency in all sections was related to the pressure which is well described in terms of density and temperature. We also explored the static limit of the stresses in the glassy state and showed that values for the stresses in this region are almost entirely dependent on the collision directions. By providing closed expressions for the constitutive relations for the stresses, energy flux and dissipation, it is hoped that we have fulfilled our objective to provide useful constitutive relations that might be suitable for fully solving the stress tensor and the

energy flux in granular flows. However, as granular systems are not in any sort of true equilibrium state further research is necessary to determine if the relations that were found to work well for our chute simulations can be easily applied to other geometries.

Probably the most important aspect that has been neglected is the rotational degrees of freedom of the grains. The dissipation in these degrees of freedom from friction during a collision would give an additional factor that may give rise to anisotropic stresses that often accompany granular flow. While frictionless bead packs can have macroscopic friction [31] the presence of microscopic static friction may still change the macroscopic observables. This will be an interesting point to investigate in future work.

ACKNOWLEDGMENTS

We acknowledge insightful conversations with Dr. N. Menon and Dr. J. R. de Bruyn. This work was supported by the Natural Science and Engineering Research Council of Canada, the Ontario Graduate Scholarship Program, and SharcNet.

[1] R. A. Bagnold, Proc. R. Soc. London, Ser. A **225**, 49 (1954); **295**, 219 (1966).
[2] S. B. Savage, J. Fluid Mech. **92**, 53 (1979).
[3] S. B. Savage and D. J. Jeffrey, J. Fluid Mech. **110**, 255 (1981).
[4] C. K. Lun, S. B. Savage, D. J. Jeffrey, and N. Chepurniy, J. Fluid Mech. **140**, 223 (1984).
[5] J. T. Jenkins and S. B. Savage, J. Fluid Mech. **130**, 187 (1983).
[6] N. Menon and D. J. Durian, Science **275**, 1920 (1997).
[7] The theory of Savage and colloborators actually uses the characteristic shear velocity to be $a\gamma$ where a is the particle diameter and γ the shear rate. This would be proportional to the mean flow velocity in a system of fixed width.
[8] J. J. Drozd and C. Denniston, Phys. Rev. E **78**, 041304 (2008).
[9] S. N. Coppersmith, C.-h. Liu, S. Majumdar, O. Narayan, and T. A. Witten, Phys. Rev. E **53**, 4673 (1996); C.-H. Liu, S. R. Nagel, D. A. Schecter, S. N. Coppersmith, S. Majumdar, O. Naryan, and T. A. Witten, Science **269**, 513 (1995).
[10] M. Otto, J.-P. Bouchaud, P. Claudin, and J. E. S. Socolar, Phys. Rev. E **67**, 031302 (2003).
[11] J.-P. Bouchaud, M. E. Cates and P. Claudin, J. Physique I France **5**, 639 (1995); J.-P. Bouchaud, P. Claudin, M. E. Cates, and J. P. Wittmer, in *Physics of Dry Granular Media*, NATO Advanced Studies Institute, edited by H. J. Herrman, J. P. Hovi, and S. Luding, 1997.
[12] J. P. Wittmer, P. Claudin, M. E. Cates, and J.-P. Bouchaud, Nature (London) **382**, 336 (1996); J. P. Wittmer, P. Claudin, and M. E. Cates, J. Physique I France **7**, 39 (1997).
[13] M. E. Cates, J. P. Wittmer, J.-P. Bouchaud, and P. Claudin, Chaos **9**, 511 (1999).
[14] M. E. Cates, J. P. Wittmer, J.-P. Bouchaud, and P. Claudin, Physica A **263**, 354 (1999).
[15] S. F. Edwards and R. B. S. Oakeshott, Physica A **157**, 1080 (1989); S. F. Edwards, *ibid.* **249**, 226 (1998); S. F. Edwards and D. V. Grinev, *ibid.* **263**, 545 (1999).
[16] C. Song, P. Wang, and H. A. Makse, Nature (London) **453**, 629 (2008).
[17] G.-J. Gao, J. Blawzdziewicz, and C. S. O'Hern, Phys. Rev. E **74**, 061304 (2006); Philos. Mag. B **87**, 425 (2007).
[18] GDR MiDi, Eur. Phys. J. E **14**, 341 (2004).
[19] F. da Cruz, S. Emam, M. Prochnow, J. N. Roux, and F. Chevoir, Phys. Rev. E **72**, 021309 (2005).
[20] G. Lois, A. Lemaitre, and J. M. Carlson, Phys. Rev. E **72**, 051303 (2005).
[21] Y. Forterre and O. Pouliquen, Annu. Rev. Fluid Mech. **40**, 1 (2008).
[22] J. J. Drozd and C. Denniston, Europhys. Lett. **76**, 360 (2006).
[23] V. V. R. Natarajan, M. L. Hunt, and E. D. Taylor, J. Fluid Mech. **304**, 1 (1995).
[24] S. Moka and P. R. Nott, Phys. Rev. Lett. **95**, 068003 (2005).
[25] C. Bizon, M. D. Shattuck, J. B. Swift, W. D. McCormick, and H. L. Swinney, Phys. Rev. Lett. **80**, 57 (1998).
[26] S. Luding, E. Clement, J. Rajchenbach, and J. Duran, Europhys. Lett. **36**, 247 (1996).
[27] Reference [8] shows a plot of the average coefficient of resolution at different heights in Fig. 6(b). In the free-fall and fluid regions μ is close to μ_0 and rises close to 1 in the glassy region (for $\mu_0=0.9$, typically $\mu\approx 0.975$ in the glassy region).
[28] W. Goldsmith, *Impact* (Edward Arnold Ltd., London, 1960), pp. 262–263, 267.
[29] C. V. Raman, Phys. Rev. **12**, 442 (1918).
[30] We use units where the acceleration due to gravity $g=1$, the mean grain radius $a=1$, and the mean grain mass $m=1$. To convert to units where, say, g=9.8 m/s^2, $a=1.5$ mm$=1.5\times10^{-3}$ m, and $m=0.11$ grams$=1.1\times10^{-3}$ kg (i.e., a steel ball with mass density of 7850 kg/m^3), multiply our distance by a in meters, time by $(a/g)^{1/2}=[(1.5\times10^{-3}\ \mathrm{m})/(9.8\ \mathrm{m/s^2})]^{1/2}=0.0124$ s and masses by m in kilograms. A typical simulation run is 10^4–10^5 time units, or 2–20 min of real time for a system made up of steel balls 3 mm in diameter. For a typical run with polydisperse grains, this corresponds to 6.5×10^9 collisions.
[31] P.-E. Peyneau and J.-N. Roux, Phys. Rev. E **78**, 011307 (2008).
[32] C. Denniston and H. Li, Phys. Rev. E **59**, 3289 (1999).
[33] Z. W. Salsburg and W. W. Wood, J. Chem. Phys. **37**, 798 (1962).
[34] B. J. Alder and T. E. Wainwright, J. Chem. Phys. **33**, 1439 (1960).
[35] N. F. Carnahan and K. E. Starling, J. Chem. Phys. **51**, 635 (1969).
[36] J. K. Percus and G. J. Yevick, Phys. Rev. **110**, 1 (1958).
[37] J. A. Barker and D. Henderson, Rev. Mod. Phys. **48**, 587 (1976).
[38] N. Clisby and B. M. McCoy, J. Stat. Phys. **122**, 15 (2006).
[39] J. Kolafa, unpublished results cited in T. Boublik and I. Nezbeda, Collect. Czech. Chem. Commun. **51**, 2301 (1986).
[40] A. Malijevský and J. Veverka, Phys. Chem. Chem. Phys. **1**, 4267 (1999).

[41] W. Losert, D. G. W. Cooper, J. Delour, A. Kudrolli, and J. P. Gollub, Chaos **9**, 682 (1999).
[42] F. Rouyer and N. Menon, Phys. Rev. Lett. **85**, 3676 (2000).
[43] T. P. C. van Noije and M. H. Ernst, Granular Matter **1**, 57 (1998).
[44] T. P. C. van Noije, M. H. Ernst, R. Brito, and J. A. G. Orza, Phys. Rev. Lett. **79**, 411 (1997).
[45] R. Cafiero, S. Luding, and H. J. Herrmann, Phys. Rev. Lett. **84**, 6014 (2000).
[46] R. G. Mortimer, *Physical Chemistry*, 3rd ed. (Elsevier, London, 2008), pp. 464, 465, 470.
[47] J. P. Hansen and I. R. McDonald, *Theory of Simple Liquids*, 3rd ed. (Elsevier, London, 2006), pp. 234, 241.
[48] S. Schöllmann, Phys. Rev. E **59**, 889 (1999).
[49] C. Veje *et al.*, in *Physics of Dry Granular Media*, NATO Advanced Studies Institute Series E: Applied Science, edited by H. J. Herrmann, J. P. Hovi, and S. Luding (Kluwer, Dordrecht, 1998), Vol. 350.
[50] D. M. Mueth *et al.*, Nature (London) **406**, 385 (2000).
[51] W. Losert, L. Bocquet, T. C. Lubensky, and J. P. Gollub, Phys. Rev. Lett. **85**, 1428 (2000).
[52] L. E. Silbert, D. Ertas, G. S. Grest, T. C. Halsey, D. Levine, and S. J. Plimpton, Phys. Rev. E **64**, 051302 (2001).
[53] Note, however that we have a factor of 3 in Eq. (59) only because we have defined temperature differently from the way it was defined in Ref. [32].
[54] P. Jop, Y. Forterre, and O. Pouliquen, Nature (London) **441**, 727 (2006); J. Fluid Mech. **541**, 167 (2005).